Flow topology of deep reinforcement learning drag-reduced bluff body wakes

Corresponding author: enrico.amico@polito.it

Flow topology of Deep Reinforcement Learning drag-reduced bluff body wakes

E. Amico,[1] J. Serpieri,[1] G. Iuso,[1] and G. Cafiero[1]
Department of Mechanical and Aerospace Engineering, Politecnico di Torino, Corso Duca degli Abruzzi 24, Turin, 10129, ITALY

(Dated: 3 July 2024)

The wake topology of a bluff body, representative of a road commercial vehicle, manipulated by different control laws for pulsed jets located at the trailing edges of the model is presented and discussed. The parameters of the control laws have been identified through previous work, in which a Deep Reinforcement Learning (DRL) algorithm was trained under different conditions to achieve drag reduction first and also taking the energy budget into account. The focus of this work is to understand the mechanisms through which the DRL agent can reach the objective in four distinct cases, with different size of the state and reward definition. Planar and stereoscopic Particle Image Velocimetry measurements were carried out at different planes in the body's wake. The findings suggest that, when large drag reduction conditions are achieved, the recirculating flow bubble is shortened in the streamwise direction, the wake becomes symmetrical in the streamwise-vertical plane at the symmetry station along the cross-stream direction, and there is a substantial pressure recovery at the base of the model. In these conditions, the wake topology drastically changes with respect to that of the natural case. Conversely, when the energy budget is introduced, the modification of the recirculating flow bubble is smaller as a consequence of the reduced actuation. This study, thus, while complementing the previous work with flow physics analyses, gives valuable insights on the wake topologies to aim for when targeting pressure drag reduction through active flow control strategies.

I. INTRODUCTION

The reduction of aerodynamic drag exerted by vehicles remains an important topic for reducing of pollutants, fuel consumption, and costs. In their study, Mohamed-Kassim and Filippone [1] noted that a decrease in drag ranging from 7% to 10% corresponded to a reduction in fuel consumption ranging from 2.7% to 5.2%. The importance and immediacy of drag reduction have been amplified in recent times due to the proliferation of electric vehicles. Indeed, the need to minimize aerodynamic drag is paramount for electric vehicles to maximize the vehicle range.

When considering a typical city car, the definition of its geometry is not particularly constrained by its operation, so it is possible to choose designs that are more efficient from an aerodynamic perspective. This is further facilitated by the typical operating conditions of city cars, which operate at relatively moderate velocities. However, this is not the case for commercial transport vehicles. The need for as much volume as possible makes it difficult to optimize the geometry, due to aerodynamics considerations, which usually results in bulky shapes. In addition, the high velocities at which these vehicles usually travel, especially on highways, exacerbate the issue. It has been shown[2] that at high speeds (130 km/h), the aerodynamic drag is about 80% of the total drag, compared to 50% at low speeds (50 km/h). The constrained optimization space, coupled with the regulatory framework, makes challenging aiming at any geometry optimization for drag reduction and/or incorporation of aerodynamic appendages. There is therefore a large potential for active flow control to minimize the drag of these vehicles.

The boxed shape of transport vehicles can be schematically represented as a three dimensional bluff body which tends to generate complex wake flows[3–11]. The time-averaged velocity field is characterized by the presence of two large recirculation zones resulting from the separation of the shear layers from the top and bottom edges of the model's base[12,13]. Even in the case of an axisymmetric shape[14], the separated flow exhibits a recirculating flow region when the base is perpendicular to the body longitudinal axis.

The wake flow is significantly affected by two main factors: the square back aspect ratio $\overline{H} = H/W$ and the ground clearance ratio $\overline{G} = G/W$, where H, W are the base height and width while, G is the underbody clearance[6,8] and the overbar denotes and will denote throughout the article non-dimensional quantities.

An essential finding highlighted in Bonnavion and Cadot [6] is that, for the boat-tail geometry, the after-body generates four strong longitudinal vortices at each corner of the base, significantly impacting the closure of the recirculation bubble compared to what is observed for the square-back after body.

In Liu *et al.* [3], a conceptual flow structure model, based on their data and following in works in the literature[15–23], is proposed for a low-drag Ahmed body with a slant angle of 35°, encompassing both steady and unsteady flow structures around the body.

The interplay between the haripin vortices emanating from the recirculation bubble[17,18], the side vortices generated at the sidewalls and the lower vortex[19] are at the core of a large body of research aimed at reducing the drag of bluff bodies. Among these, active flow control approaches are reporteed in[24–27].

Li *et al.* [28] propose a control approach based on a closed-loop opposition control scheme with pulsed jets on both sides of the base. The main objective was to manipulate the wake by forcing it on either side and to ultimately achieve drag reduction. This approach is supported by the findings presented

in Barros *et al.* [7], which demonstrated that forcing at low frequencies applied on one side of the base, targeting time scales comparable to those dominating the shear layer dynamics, has the capability to reverse the wake asymmetry of the Ahmed body.

While active techniques demand a more intricate implementation, they confer the distinct advantage of geometric non-intrusiveness. Moreover, they generally yield superior drag reduction values. It is crucial to underline that, for a comprehensive evaluation of the technique, the overall efficiency must be duly considered, taking into account the power supplied to the control system in the energy budget.

Cerutti et al.[12] carried out an experimental investigation to determine the effectiveness of continuous blowing to control the near wake of a square-back road vehicle. The authors evidenced that continuous forcing can lead to drag reduction as large as $\sim 12.7\%$. They also showed that the forcing can be tailored to minimize the power consumption, leading to lower values of drag reduction $\sim 7\%$.

In the realm of fluid dynamics and control theory, the advent of Deep Reinforcement Learning (DRL) stands as a pivotal advancement, especially praised for its efficacy as a closed-loop flow control technique[29]. DRL represents a paradigm shift in flow control methodologies, leveraging the power of artificial intelligence and neural networks to navigate complex and dynamic flow environments[27,29–34]. By integrating principles from reinforcement learning with deep neural network architectures, DRL frameworks are adept at learning optimal control policies directly from observational data or simulations, without necessitating explicit knowledge of the underlying flow physics but enabling agents to learn by interacting with an environment and receiving rewards for desired behaviors.

The application of DRL to drag reduction scenarios is particularly noteworthy, as it offers a versatile and adaptive approach to mitigating aerodynamic drag. In contrast to the numerical context, where applications of DRL are prevalent, in the experimental context applications are severely limited. The use of DRL in an experimental context allows bypassing the challenges associated with high-fidelity simulations at high Reynolds numbers, although other challenges related to implementation and the need for sufficiently high sampling rates persist.

In a previous study, related to the one currently presented, Amico et al.[35] trained different DRL agents to obtain forcing conditions leading to the drag reduction scenario of the same commercial road vehicle of Cerutti *et al.* [12] by means of 4 pulsed jets, one per edge of the model base, with adjustable exit velocity (U_j) and pulsation frequency (f_j). The authors explored the effect of the dimension of the state and the reward definition on the optimal forcing. The investigated cases, with the definitions of the state and reward, are summarized in Table I. The results showed the agent's capability to adapt to changed reward definitions. In particular, a first agent was trained to maximize a reward (r) defined as

$$r = Cd_0 - Cd = \Delta Cd \tag{1}$$

where Cd and Cd_0 are the drag coefficients in the forced and unforced conditions, respectively.

The efficiency is defined as suggested by Englar[36], who analysed the receptivity of the wake with respect to the variation of the drag coefficient and the jet momentum coefficient C_μ:

$$\frac{\Delta Cd}{C_\mu} = \frac{D_0 - D}{\frac{1}{2}\sum_{j=1}^{N_{jets}} \rho A_j {U_j}^2}. \tag{2}$$

where ρ is the air density, A_j is the cross-section of the j-th jet, V_j is the exit velocity of the j-th jet and D and D_0 are the drag in the forced and unforced conditions, respectively. The denominator term takes into account the amount of momentum associated with the jets.

The result of eq. 2 can take both positive and negative values; in particular, drag reducing configurations are associated to positive values. Furthermore, values of $\frac{\Delta C_d}{C_\mu} > 1$ correspond to energy-efficient configurations.

For two different cases (3 and 4, see Table I), the agent was trained to account for the efficiency by introducing a penalization term k_μ in the definition of the reward, as it is customary for DRL applications[26,30]:

$$r = Cd_0 - Cd + k_\mu = \Delta Cd + k_\mu \tag{3}$$

with k_μ

$$k_\mu = \frac{1}{10}\sum_{j=1}^{N_{jets}} \frac{V_k - \overline{V}_j}{V_{max}} \tag{4}$$

where V_k and V_{max} are respectively equal to 6.5 V and 9.5 V and correspond to the reference voltage value and to the higher value of the voltage supplied to the solenoid valves for controlling the pulsed jets. The coefficient 1/10 is used to make comparable the values of k_μ and of ΔCd. Greater values of this coefficient may favour energy efficient or ineffective control strategies. The control voltage of the solenoid valves is linearly related to the speed, as reported in Cerutti [37].

The training of the agent is conducted using two distinct state definitions, as outlined in Table I. The state is characterized by the distribution of the pressure coefficient Cp on the base of the model.

$$Cp = \frac{< p > - < p_\infty >}{0.5 \cdot \rho \cdot U_\infty^2} \tag{5}$$

where the subscript ∞ indicates freestream conditions and the symbol <> indicates the mean value.

Subsequently, this definition is expanded by incorporating fluctuating pressure (p') via Cp_{RMS}.

$$Cp_{RMS} = \frac{\sqrt{< p'^2 >}}{0.5 \cdot \rho \cdot {U_\infty}^2} \tag{6}$$

	State	Reward
Case 1	Cp	ΔCd
Case 2	Cp+Cp_{RMS}	ΔCd
Case 3	Cp	ΔCd+k_μ
Case 4	Cp+Cp_{RMS}	ΔCd+k_μ

TABLE I: Summary of the state and the reward definitions explored in[35].

In the case of maximum drag reduction, the agent learned strategies to achieve drag reductions as large as 10%, with values of $\frac{\Delta C_d}{C_\mu}$ of 5. In Case 3 and Case 4 the agent attains lower values of drag reduction (approximately 5%) and greater efficiency (around 10).

The present investigation builds upon the mentioned results[35] to provide insights on the near-wake structure stemming from the four aforementioned control strategies.

The paper is structured as follows: the experimental set-up is described in section II. The baseline flow is described in the section III A and, in section III B, the forced conditions are analyzed and compared with the baseline flow. The flow control mechanisms are discussed in section III C. In section IV the conclusions of the work are drawn.

II. EXPERIMENTAL SETUP

A. Wind tunnel and model

The experiments are carried out in the open-circuit wind tunnel at Politecnico di Torino[12,13,35]. The flow is accelerated and conveyed to the test section through a convergent duct. The rectangular test section (0.9 m and 1.2 m wide) is 6.5 m in length with a small divergence angle of 0.1° to account for the growth of the boundary layer on the walls.

The free-stream is characterized by a turbulence intensity (TI), defined as $TI = \frac{u'_{rms}}{U_\infty} * 100$, equal to 0.35%.

The model used[12,13,35] is a 3D printed square-back road vehicle, see Figure 1, typically employed as heavy-duty vehicle, with length (L), width (W) and height (H) equal to 412 mm, 170 mm and 200 mm, respectively.

The model is positioned with a vertical strut connected to its roof. The strut, which acts as a mechanic amplifier, is embedded in an aerodynamically shaped wing profile (NACA 0020, with $c/W = 0.07$, where c is the airfoil's chord) and it rigidly connects the model to a one-axis load cell located outside the test section to perform the drag measurements. The strut fairing is also used to carry the pneumatic lines that supply the jet's air and the necessary wirings for the pressure scanner, microphone probes and the DAQ acquisition boards. The model is positioned to keep a gap between the underbody and the wind tunnel floor of $\overline{G} = 0.1$. The frontal area of the model is 3.1% of the cross-section of the wind tunnel (this value increases to 4.5% when considering also the strut fairing).

The positioning of the model in the wind tunnel is carefully defined to account for several issues that are typical of automotive testing. The absence of the moving floor inevitably modifies the structure of the underbody flow. While this can be a significant issue when performing downforce measurements, its effect on the measurement of the drag is much less relevant. A large number of investigations are indeed performed with a stationary floor and steady wheels[8,9,38]. Wang et al.[39] carried out a comparison of wind tunnel data obtained on the model employed for the present investigation with numerical simulations to quantify this effect. The authors confirmed that the main effect is on the lift coefficient whereas the effect on the drag coefficient is within 5% compared to a configuration where the moving floor is employed.

The growth of the boundary layer on the wind tunnel floor has been minimized by implementing a suction slit at about two model's lengths upstream of the model's nose. The resulting boundary layer integral parameters, as measured by dedicated hot wire anemometry experiments, are such that $\delta^*/G = 0.07$, with δ^* being the displacement thickness of the boundary layer. This value is in good agreement with other investigations performed with a stationary floor[4].

All the tests are conducted at $Re = \frac{U_\infty \cdot L_{ref}}{\nu} \sim 10^5$, with $L_{ref} = \frac{H+W}{2} = 0.185$ m and $U_\infty = 9.1$ m/s being the freestream velocity. The model is instrumented with static pressure taps located at the base. The pressure signals are acquired using acrylic tubes connected to a Scanivalve pressure scanner (ZOC33) with SmartZOC 100. The pressure scanner has a full-scale (FS) of ± 2.5 kPa, with accuracy of 0.15% FS. The pressure signals are sampled at a frequency of 50 Hz for 20 seconds, thus ensuring statistical convergence.

Furthermore, the back of the vehicle is populated with 16 Electret microphone probes whose electric signals are acquired with National Instruments DAQ boards (NI-9215). The microphonic probes were previously calibrated against a high sensitivity microphone Bruel and Kjaer 4939. The microphone signals were acquired at a frequency of 2 kHz for 40 seconds.

B. Flow actuation system

The drag measurements were performed using a one-axis Dacell UU-K002 load cell with a full scale FS = 2 Kg_f and a rated output equal to 1.5 $mV/V \pm 1\%$. The excitation voltage was set to 10 V using a stabilized AL862D 0-30 V power supply. The output signal is then amplified using a dedicated conditioning module.

The forcing is obtained by four air jets slits located along the edges of the model's base, as schematically depicted in Figure 2. Each actuator is a cylinder with a rectangular slit of 1 mm along its length, as the one implemented in previous investigations[12,13,35,40]. In the present case, a fixed injection angle of 65° towards the centre of the wake is considered. The slits have a length of 104 mm in the case of the top and bottom slits, and 132 mm in the case of the lateral slits.

A schematic representation of the air supply that feeds the jets is reported in Figure 2. A pneumatic line with a maximum operating pressure of 10 bars feeds the system. The flow rate supplied to each of the jets was measured using three inde-

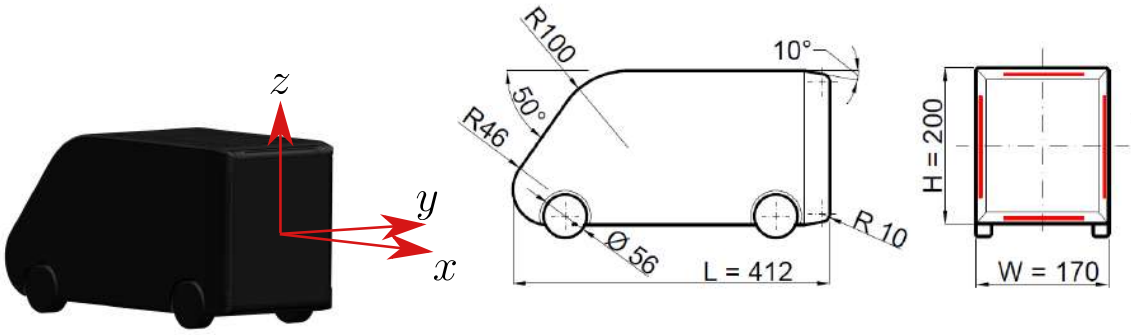

(a) (b) (c)

FIG. 1: Schematic representation of the wind tunnel model used for experiments: a) isometric view with the indication of the reference frame; b) side view and c) back view. The colored continuous lines represent the injection slits of the active flow control system. Dimensions are in mm.

pendent flow meters (model IFM Sd8000). The flow control system is designed in a way such that it allows the independent activation of the top, bottom and lateral jets.

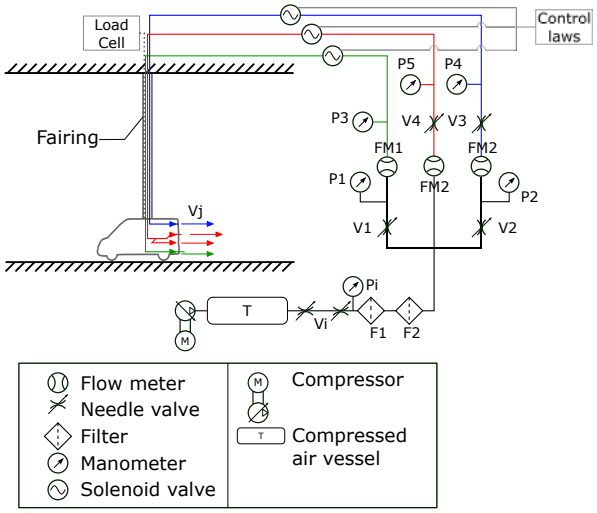

FIG. 2: Schematic representation of the jets' air supply system.

The flow rate was varied using three solenoid valves that can be modulated according to different control laws. It must be specifically noted that the lateral jets are connected to the same valve and, as such, were actuated according to the same control law.

The control laws were of the form:

$$V_j = \frac{V_{jmax} - V_{min}}{2} \cdot sin(2\pi f_j \cdot t) + \frac{V_{jmax} + V_{min}}{2} \qquad (7)$$

where j indicates the lateral, top or bottom jet. V_{min} represents the minimum operating voltage of the valve (equal to 5.5 V) V_j the amplitude selected by the agent and f_j the frequency of the actuation. Following eq. 8 and eq. 9 the amplitude and frequency were normalised to attain values between ± 1[41,42].

$$A_{e_j} = 2 \cdot \frac{V_{jmax} - V_{min}}{V_{max} - V_{min}} - 1 \qquad (8)$$

$$A_{f_j} = 2 \cdot \frac{f_j - f_{min}}{f_{max} - f_{min}} - 1 \qquad (9)$$

where V_{max} = 9.5 V, f_{max} = 30 Hz and f_{min} = 0 Hz, owing to the working envelope of the valves. When each of the two parameters attains a value equal to -1, this corresponds to a null value of the voltage or frequency, while when it attains a value of 1, the voltage and the frequency are maximum. Furthermore, the condition $A_f = -1$ corresponds to the case of a steady jet injection.

C. Flowfield measurements

Velocity field measurements were performed in the vehicle wake by means of PIV (Planar Particle Image Velocimetry) and sPIV (Stereoscopic Particle Image Velocimetry), as sketched in Figure 3. The PIV measurements were instead carried out at the symmetry plane $\frac{y}{W} = 0$. The sPIV measurements were carried out at five different streamwise locations ($\frac{x}{W} = 0.15, 0.4, 0.6, 0.8, 1.0$).

The illumination of the tracer particles is obtained using a Dantec Dynamics Dual Power Nd:YAG laser characterized by 200 mJ/pulse and 15 Hz maximum repetition rate. The laser beam was shaped into a sheet having a thickness of about 1 mm, using a spherical and a cylindrical lens.

The flow was seeded upstream of the stagnation chamber using HAZEBASE fluid. The liquid droplets of 1 μm in diameter were generated using a Safex Fog generator FOG 2010.

The PIV and sPIV images were captured using two Andor sCMOS 5.5 Mpx cameras each equipped with a Tokina 100 mm Macro lens equipped with Scheimpflug mounts to ensure a uniform focusing. The resulting digital resolution was 13pix/mm and 15pix/mm for the PIV and sPIV measurements, respectively.

The field of view is 1.1x1W in the xz plane for the PIV measurements, while it is 0.71x0.81W in the yz plane for the sPIV measurements.

For each test, 2000 image pairs were captured, which ensured the convergence of the relevant statistics.

A POD based filter[43] was implemented to mitigate the effect of the laser reflections on the wind tunnel walls and on the model. This approach demonstrated to be much more effective than the minimum subtraction. Images deformation and velocity vector fields interpolation was carried out using third order spline functions[44,45]. A Blackmann weighting window is used during the correlation process to tune the spatial resolution of the PIV process[46].

A geometric calibration of one camera for the PIV measurements and of the two cameras for the sPIV measurements was performed. Images of a double plane target with white dots on a dark background were acquired and then used to perform the calibration with a pin-hole model. The resulting root mean square of the error was of about 1 pixel on each camera. A self-calibration[47,48] was also performed to further reduce the residual error below 0.1 px.

A multi-step algorithm was implemented to perform the cross-correlation, and the final interrogation window size was 16x16 pixels, with 50% overlap, thus yielding a vector spacing of 0.61 mm (PIV) and 0.55 mm (sPIV).

Owing to the wake symmetry with respect to the xz plane[39], reflectional symmetry was enforced by averaging out the velocity fields obtained with the sPIV measurements for values of $y > 0$ and $y < 0$.

III. RESULTS

A. Baseline flow

In this section, the wake topology for the unforced (baseline) case is discussed. In the following, the superscript $\bar{\cdot}$ indicates normalization with respect to the freestream speed U_∞ or the model's width W for velocities and lengths, respectively. All quantities reported are intended to be averaged over time. We will denote u as the streamwise velocity (along x), v as the cross-stream velocity (along y) and w as the vertical velocity (along z).

The streamwise and vertical velocity components measured in the model's symmetry plane ($y/W = 0$) are presented in Figures 4a and 4b. As it is expected[7,39], a region of negative streamwise velocity ($\overline{u} < 0$) indicates the existence of a bubble of recirculating flow, see Figure 4a. The $\overline{u} = 0$ iso-line (the dashed white line in Figure 4a) allows us to identify the streamwise extension of this region in that plane. The recirculating flow results to be embedded within two regions of positive streamwise velocity, representing the underbody flow and the flow detatching from the model's roof. In order to characterize the recirculating flow, two quantities are introduced: the centroid of the region with $\overline{u} < 0$ (the bubble) and the length of the recirculating flow $\overline{B}_L$, defined as the maximum streamwise extent of this region, measured from the model base.

The time-averaged vertical velocity $\overline{w}$ is reported through colormaps in Figure 4b. The distribution shows a large asymmetric clockwise recirculating motion owing to the presence of the ground. The results in terms of $\overline{u}$ and $\overline{w}$ are in agreement with the previous investigations[7,39]. The interplay between the recirculating flow and the shear layers originating at the top and bottom edges of the model base leads to the formation of two vortical structures: a first one V_b, that is close to the base, whose centre is located at $x = 0.18$ and near the top edge; a second one, much smaller in size, located farther downstream. This is not properly captured with the present investigation due to limited spatial resolution, but discussed in literature[7,39].

The pressure distribution on the base of the model is displayed in Figure 4c in terms of pressure coefficient Cp. The spatially averaged pressure coefficient calculated across the base is equal to $Cp_b = -0.12$, in good agreement with previous measurements in the literature[8,12,13], for similar values of the aspect ratio of the model's geometry and of the Reynolds number. The pressure distribution on the base of the model is consistent with this recirculating motion (see Figure 4b and 4c). A high pressure region is identified for $\overline{z} < 0$, corresponding to the impingement of the lower part of the recirculation region. The downward directed pressure gradient is then associated with the upward motion of the recirculating flow.

The centroid of the pressure distribution has been shown to be related with the mechanism leading to drag reduction[49]. Therefore, in Figure 4c, the location of the centroid calculated as in eqs. 10 and 11, considering only half of the base in the $\overline{y}$-direction, is shown with a yellow marker and $\overline{z_G}$ attains a value of 0.03.

$$\overline{y_G} = \frac{\sum_{n=1}^{N} y_i \cdot Cp(y_i, z_i)}{\sum_{n=1}^{N} Cp(y_i, z_i)} \tag{10}$$

$$\overline{z_G} = \frac{\sum_{n=1}^{N} \overline{z_i} \cdot Cp(y_i, z_i)}{\sum_{n=1}^{N} Cp(y_i, z_i)} \tag{11}$$

The streamwise ($\overline{u'u'}$), vertical ($\overline{w'w'}$) and cross components ($\overline{u'w'}$) of the Reynolds stress tensor are presented in Figure 5. The component $\overline{u'u'}$ (Figure 5a) exhibits two regions of maxima in correspondence of the top and bottom shear layers, related to the shear layers developing between the wake flow and the flow emerging from the underbody/roof of the model. On the other hand, the vertical component of the velocity variance $\overline{w'w'}$ (Figure 5b) attains large values at the centre of the recirculating flow ($\overline{z} = 0$), suggesting that the wake is meandering leading to strong fluctuations in the wall-normal direction is occurring.

The $\overline{u'w'}$ component (Figure 5c) is instead characterized by negative and positive peaks in correspondence of the top and

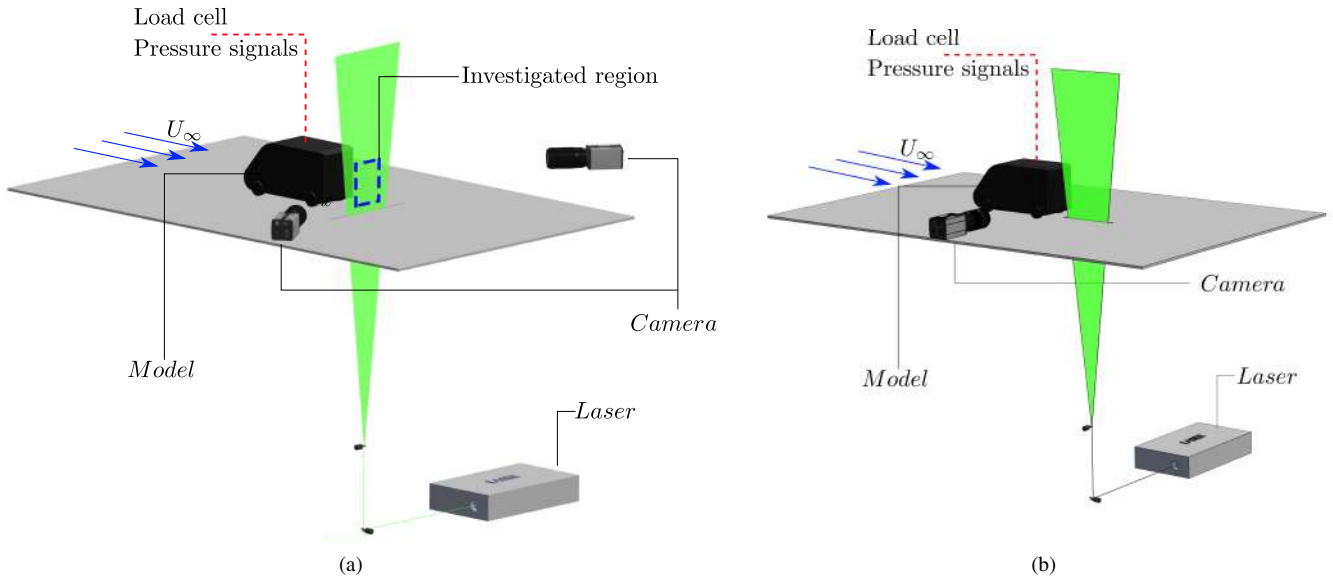

FIG. 3: Schematic representation of sPIV (a) and PIV (b) experimental setup.

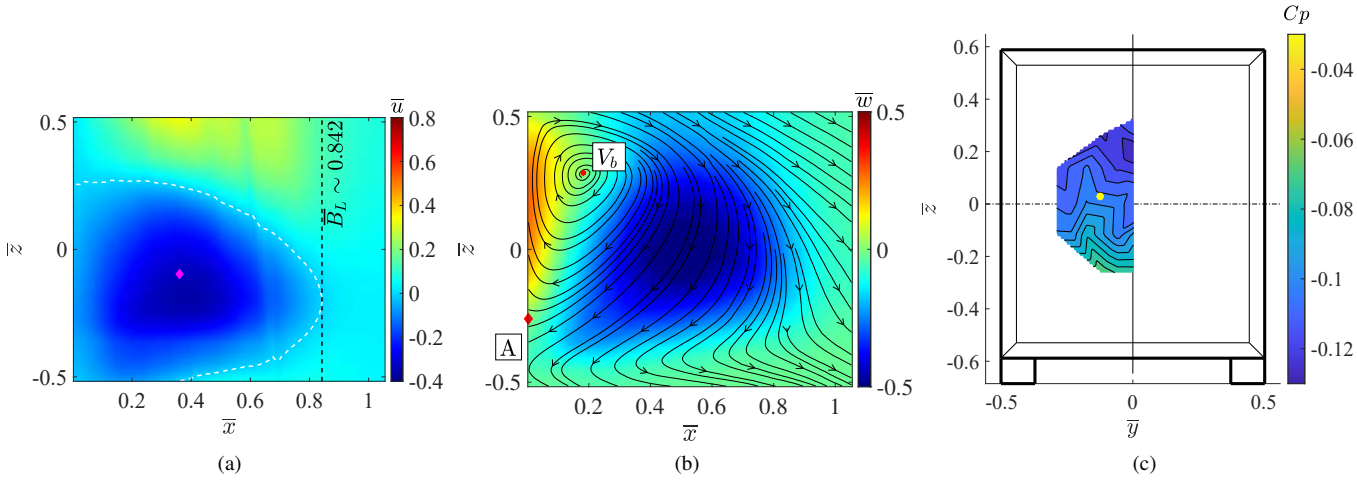

FIG. 4: Colormaps of time-averaged velocity: (a) streamwise velocity component, indication of the wake centroid along with the iso-line of $\overline{u} = 0$ (white dashed line) and the indication of the wake streamwise extent $\overline{B}_L$ (black dashed line), (b) vertical velocity component ($\overline{w}$) with overlaid $u - w$ streamlines of in-plane velocity, measured in the xz plane ($\overline{y} = 0$). (c) Pressure coefficient distribution on the model base.

bottom shear layers, respectively. In particular, the shear layers are characterized by an inward spreading (i.e. towards the centre of the wake) giving rise to negative/positive values of $\overline{u'w'}$.

The streamwise velocity component measured at $\overline{x} = 0.15, 0.4$, 0.6, 0.8 and 1.0 by sPIV, with overlaid streamlines ($v - w$) are shown in Figure 6.

At $\overline{x} = 0.15$ (Figure 6a), the streamline are consistent with the presence of the recirculating flow, out of the measured plane, thus evidencing the presence of a source in the measured plane. In all the remaining locations (Figures 6b, 6c, 6d and 6e), the flow shows the presence of two vortical structures originating from the interplay between the wake flow and the surrounding flow. It is noteworthy mentioning that the vortical structures labelled in Figure 6 will be further discussed in section III C.

A three-dimensional reconstruction of the near wake of the model obtained by interpolating with linear functions the measured sPIV planes is shown in Figure 7. In this figure, in order to show more interesting flow features, we exploit the flow symmetry with respect to $\overline{y} = 0$ plane. Accordingly, some feature are shown on the $\overline{y} > 0$ side while other on the $\overline{y} < 0$ side (and it is left to the reader to project the shown features on the other side taking into account for the due sign change).

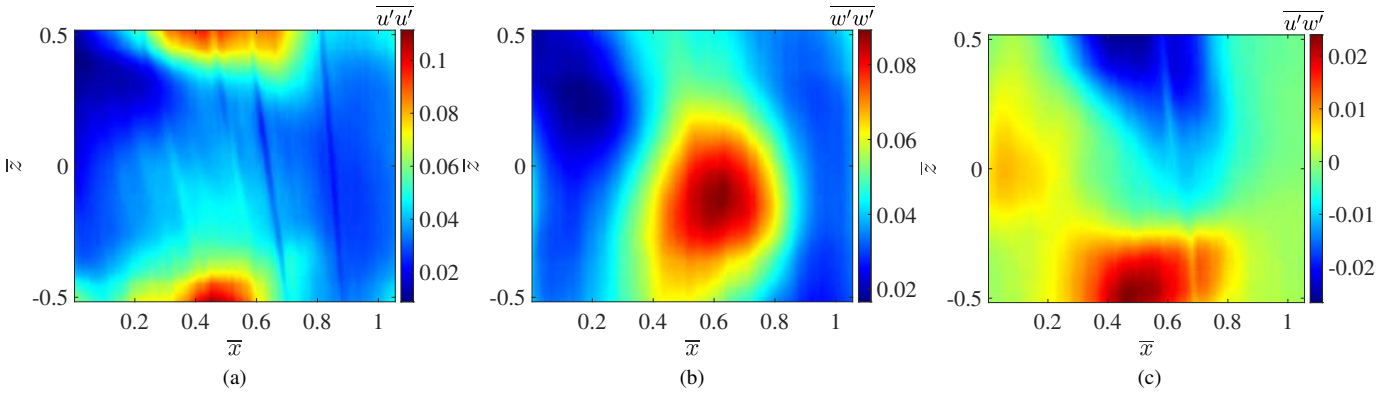

FIG. 5: Colormaps of time-averaged velocity: (a) streamwise and (b) cross-stream components of the velocity variance. (c) Streamwise-cross velocity covariance measured in the xz plane ($\bar{y} = 0$).

In particular, Figures 7a, 7b and 7c display the lateral, rear and top views of the flow, while Figure 7d shows the isometric view. The iso-surface of $\overline{u} = 0$ is reported in blue, albeit blanked for values of $\bar{y} > 0$ to improve the readability of the plots. The Q-criterion is applied to the three-dimensional flow field, to highlight the spatial arrangement of the vortical structures that populate the wake. In particular, of the regions with value of $Q >= 10^3$, in Figure 7 are displayed those with values of $\overline{\omega_x} > 0$, color coded in yellow. In Figure 7, a downward evolution of the streamwise structure is shown, originating from the roll-up of the shear layers embedding the wake. The green, red and magenta isosurfaces are color-coded according to $\overline{u'w'} < 0$, $\overline{u'w'} > 0$ and $\overline{u'v'} > 0$, respectively. They highlight that the evolution of the shear layer is inward spreading, thus contributing to the closure of the bubble.

The identified isosurfaces allow us to delineate the characteristics of the recirculation zone as highlighted earlier and this analysis allows us to confirm that the isosurface $\overline{u} = 0$ identifies the recirculation region. Therefore, for simplicity of exposition, only the isosurface $\overline{u} = 0$ will be used below to identify the recirculation region.

The sPIV measurements give us access to some terms of the turbulence production $\overline{\mathcal{P}} = -\overline{u_i' u_j'} \frac{\partial \overline{U}_i}{\partial x_j}$ and the turbulence kinetic energy $\overline{q^2} = \frac{1}{2} \sum_{i=1}^{3} \overline{u'_i}^2$, limited to $\bar{y}$ and $\bar{z}$ directed gradient.

The $\overline{\mathcal{P}}$ fields are depicted in Figures 8a-8e for $\bar{x} = 0.15, 0.4, 0.6, 0.8$, and 1.0 with overlaid isolines of $\overline{q^2} = 0.08, 0.15$, and 0.30. A $\bar{x} = 0.15$ the production term exhibits a broad negative region, indicating that the mean flow extracts energy from the turbulence. Moving downstream, $\bar{x} = 0.15$, the production increases, attaining $\overline{\mathcal{P}} > 0$ at the symmetry plane only beyond $\bar{x} \sim 0.6$, see Figure 8c. It is also worth mentioning that the maximum value of production, within the investigated flow domain, is obtained near the closure of the recirculating flow bubble, i.e. for $0.8 < \bar{x} < 1$, see Figures 8d and 8e. This suggests that this is a region of intense shear and Reynolds stresses, which in turn give rise to turbulence production.

Regarding $\overline{q^2}$, a different trend is observed. Moving from $\bar{x} = 0.15$ in Figure 8a to $\bar{x} = 0.4$ in Figure 8b, there is a decrease in the extent of the lateral regions of $\overline{q^2}$. However, for $\bar{x} > 0.4$, a consistent increase in $\overline{q^2}$ is evident, as seen in Figures 8c, 8d, and 8e. This can be explained by considering the shear layers that originate at the edges of the base, which enclose the recirculating flow bubble. As the flow evolves downstream, these shear layers subtract energy from the mean flow and contribute to the turbulence production. The region immediately downstream of the body initially experiences a high level of turbulent kinetic energy due to the pressure gradient and the flow is pushed towards the high-pressure zone, leading to an initial increase in turbulent kinetic energy. However, immediately downstream of the body, the mean flow drains energy from the turbulence as a result of the action of the low pressure, causing a reduction of $\overline{q^2}$ at $\bar{x} = 0.4$, see Figure 8b.

B. Wake topology of the DRL-controlled flows

In this section, the near wake configuration resulting from the four forcing conditions found by the agents trained through DRL in Amico et al.[35] are analyzed. Tables II and III summarise the forcings considered in the present investigation, in terms of the amplitude (eq. 8) and frequency (eq. 9) of the actuation parameters (Tab. II) and in dimensionless units (Tab. III), respectively. The resulting drag reduction and efficiency related to the control scenarios are also reported for completeness in Tab II.

In particular, we will consider two conditions where the DRL algorithm was trained to achieve maximum drag reduction with no constraints on the power expense, referred to as Case 1 and Case 2 for simplicity, whereby Case 2 is characterized by a broader state definition (as reported in Table I). In Case 1, the state comprises of the static pressure coefficient Cp on the model base, whereas in Case 2, the fluctuating pressure coefficients Cp_{rms} measured on the base are added. We will also consider two conditions where a penalization term was added to take into account the power spent in the actuation

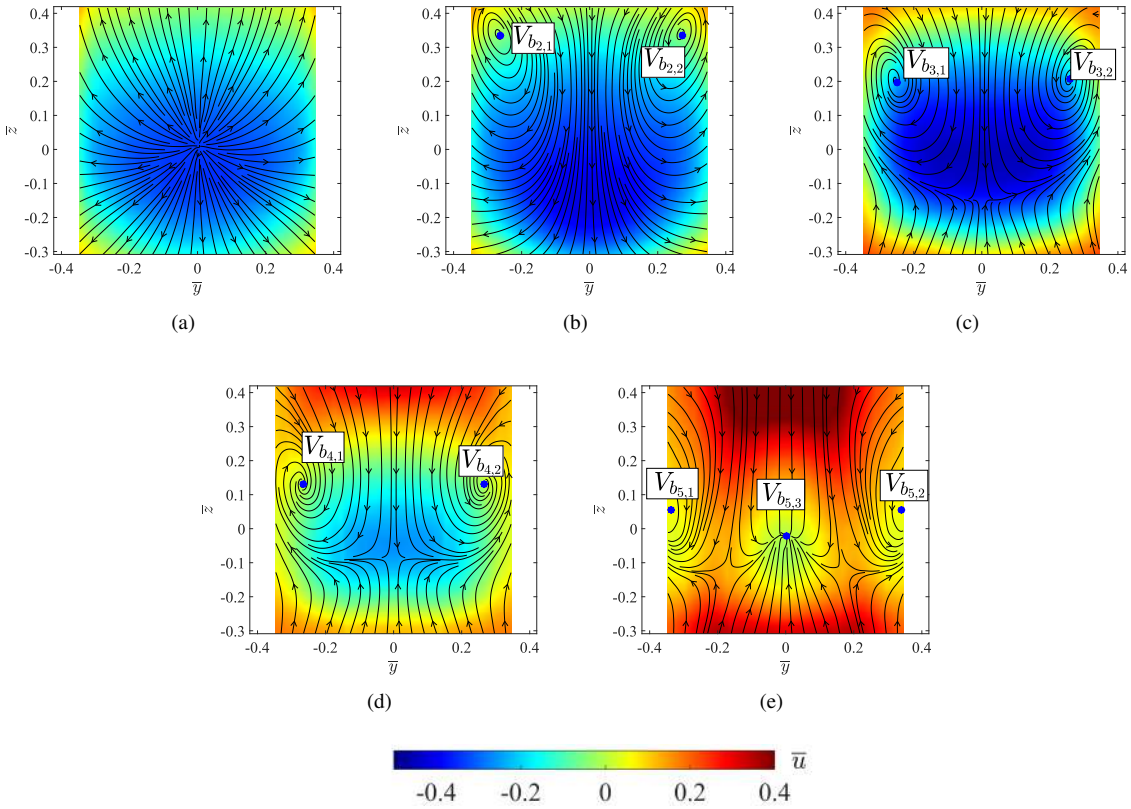

FIG. 6: Colormaps of streamwise time-averaged velocity $\overline{u}$ field at $\overline{x} = 0.15(a), 0.4(b), 0.6(c), 0.8(d), 1.0(e)$, view from downstream, with $v-w$ streamlines (in black).

(eq. 3), referred to as Cases 3 and 4 where, again the difference between Case 3 and Case 4 refers to the state definition as for Case 1 and Case 2. Cases 1 and 2 show a very similar maximum drag reduction value (about 10%), while Cases 3 and 4 show a drag reduction value of about 3.5% and 5%, respectively. For more information on the different definitions of the two agents, please refer to Amico et al.[35].

	Case 1		Case 2		Case 3		Case 4	
	A_e	A_f	A_e	A_f	A_e	A_f	A_e	A_f
Lateral	0.93	-0.98	0.8	-0.98	-0.28	0.99	0.31	-0.99
Bottom	-0.47	0.99	-0.23	0.9	-0.28	0.69	-0.84	-0.52
Top	-0.99	-0.12	-0.9	-0.98	-0.95	0.43	-0.99	-0.86
$\overline{DR}$	$\sim 10\%$		$\sim 10\%$		$\sim 5\%$		$\sim 6\%$	
$\Delta Cd/C_\mu$	~ 7		~ 7		~ 9.7		~ 8.9	

TABLE II: Summary of the non adimensional parameters A_e and A_f used in the forcing law and the DR ed $\Delta Cd/C_\mu$ attained[35].

For Case 1, Case 3 and Case 4, (see Tables II and III), the agent identified the effect of the top jet as detrimental and as such it turned it off. The result is in agreement with the open loop studies presented by Cerutti et al[12]. It should be considered that the identified forcing conditions can likely be also influenced by the presence of the strut. Different is for Case 2 where, from the top jet, is introduced flow with velocity equal to $\sim 0.15\ U_\infty$, see Table III. The significant disparity between the two control laws under the condition of maximum drag reduction, Case 1 and Case 2, is characterized by a decrease in laterally introduced flow rate but an increase in both upper and lower jet velocities, as presented in Tables II and III. Notably, for Case 2, the upper jet not only activates but also synchronizes with the lateral jet, both operating at $\overline{f} = St = \frac{f \cdot W}{U_\infty} \approx 0.01$. Conversely, the lower jet pulses at $\overline{f} \approx 0.56$ in both Case 1 and Case 2.

Case 3 is characterized by large values of flow rate from the lateral and bottom jets. On the other hand, in Case 4, there is essentially a lateral actuation, with the bottom jet very close to being switched-off. Nonetheless it is important to note that, despite the two completely different forcing conditions, the drag reduction values are very similar, as reported in Table II. This is not surprising: given the complexity of the parametric space, it is indeed expected that the resulting actuation law might represent a local optimum.

In all the identified situations, a decrease in drag is observed, consistent with the findings of Haffner *et al.*[49]. Specifically, referring to Figure 4c, it is evident that for the baseline case, the center of pressure CoP has a value of $\overline{z_G} > 0$. In Figure 9c, 9f, 9i the colormaps of the pressure coefficient measured at the model's base are reported. All the forced

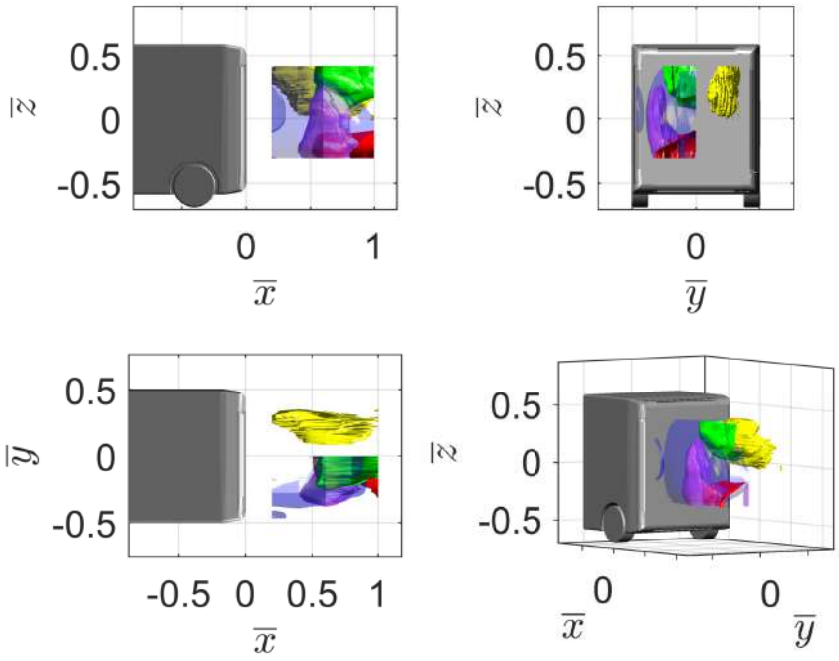

FIG. 7: Projections and isometric views of the three-dimensional flow structures in the near wake of the model. Iso-surface of $\overline{u} = 0$ (in blue) representative of the recirculating flow bubble. Iso-surface of $Q = 10^3$, color-coded in yellow for values of $\overline{\omega_x} > 0$; green (red) iso-surfaces of $\overline{u'w'} < (>)0$ (respectively). Magenta iso-surface of $\overline{u'v'} < 0$.

	Case 1			Case 2			Case 3			Case 4		
	$\overline{V}_{max}$	$\overline{V}_{min}$	$\overline{f}$	$\overline{V}_{max}$	$\overline{V}_{min}$	$\overline{f}$	$\overline{V}_{max}$	$\overline{V}_{min}$	$\overline{f}$	$\overline{V}_{max}$	$\overline{V}_{min}$	$\overline{f}$
Lateral	1.60	0.00	0.01	1.47	0.00	0.01	0.50	0.00	0.55	1.06	0.00	0.01
Bottom	0.85	0.00	0.56	1.42	0.00	0.56	1.32	0.00	0.46	0.23	0.00	0.14
Top	0.02	0.00	0.24	0.15	0.00	0.01	0.02	0.00	0.39	0.02	0.00	0.52

TABLE III: Summary of the adimensional control parameters $\overline{V}_{max}$, $\overline{V}_{min}$ and $\overline{f}$.

cases are characterized by a downward shift of the centre of pressure. This result is in agreement with what was presented by Haffner *et al.* [49] who suggested that an effective forcing is obtained when the forcing is operated in the opposite direction to that of the *CoP* position vector.

Analyzing the colormaps of the normalized time-averaged streamwise velocity (see Figures 9a, 9d, 9g and 9j) and cross-stream velocity (see Figures 9b, 9e, 9h and 9k), the effect of the actuation is evident, as it causes an anticipated closure of the recirculation bubble. This can be appreciated by observing the value of $\overline{B}_L$, which for Case 1, Case 2 and Case 3 reaches values close to 0.5, compared to 0.85 in the unforced case. On the other hand, Case 4 features a wake structure similar to the unforced case. These differences can be justified in the light of the previous consideration on the forcing conditions. In fact the bottom jet has the greatest influence on the recirculating flow, as previously evidenced by Cerutti et al.[13], and it is turned off for the Case 4. It is also important to highlight that these results do not show a direct correlation between the size of the recirculating zone and the measured drag. The angle ξ, representing the orientation angle of the high momentum flow resulting from the interaction between the bottom jet and the underbody flow is also reported in Figure 9 for the Case 1, Case 2 and Case 3. This is evaluated by calculating the angle between the x-axis and the major axis of the ellipse that has the same second moments of the region where $\overline{u} > 0.8 \cdot max(\overline{u})$. In addition to observing the trace of the forcing conditions through regions of high $\overline{u}$ velocity in Figures 9a, 9d and 9g, it is noteworthy to observe the introduction (in Case 1, Case 2, and Case 3) of zones of counter-clockwise rotation (see Figures 9b, 9e, 9h and 9k). This is caused by the bottom jet, which energizes the shear layer that develops from the lower side of the base, thus leading to an anticipated interaction with the shear layer originating from the opposite side. In these conditions (Case 1, Case 2 and Case 3), there are two different recirculating regions (Figures 9b, 9e and 9h): a first region, reduced in size and displaced upwards, ($V1_{up}$,$V2_{up}$ and $V3_{up}$ respectively for Case 1, Case 2 and Case 3), also evidenced in

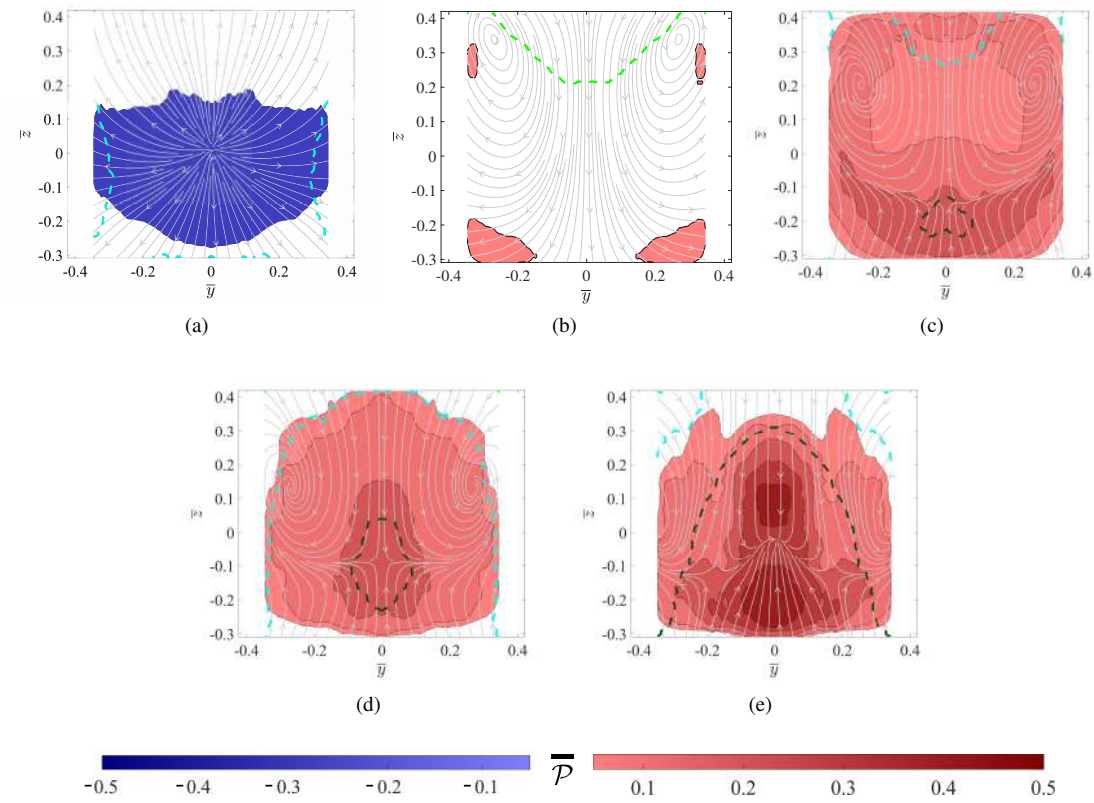

FIG. 8: Colormaps of $\overline{\mathcal{P}}$ at $\overline{x} =$ 0.15(a), 0.4(b), 0.6(c), 0.8(d), 1.0(e) with overlaid $v-w$ streamlines and $\overline{q^2}$ isolines for $\overline{q^2} = 0.08$ (light green), 0.15 (light blue), and 0.30 (dark green).

	Case 1		Case 2		Case 3		Case 4	
	$\overline{Q}_{max} \cdot 10^3$	$\overline{Q}_{mean} \cdot 10^3$	$\overline{Q}_{max} \cdot 10^3$	$\overline{Q}_{mean} \cdot 10^3$	$\overline{Q}_{max} \cdot 10^3$	$\overline{Q}_{mean} \cdot 10^3$	$\overline{Q}_{max} \cdot 10^3$	$\overline{Q}_{mean} \cdot 10^3$
Lateral	7.12	3.53	6.72	3.42	2.20	1.00	4.82	2.23
Bottom	3.05	1.47	5.05	2.38	4.7584	2.23	0.83	0.50
Top	0.07	0.07	0.52	0.29	0.09	0.08	0.07	0.06
Total	10.32	5.14	12.83	6.38	7.14	3.38	5.78	2.85

TABLE IV: Maximum and medium flow rates for the side, lower and upper jets normalised with respect to the freestream velocity and the model width.. Total means the maximum flow rate obtained by summing the identified control laws.

the unforced case (V_b in Figure 4b), with a clockwise rotation. A second region ($V1_{down}$,$V2_{down}$ and $V3_{down}$ respectively for Case 1, Case 2 and Case 3), with a counter-clockwise rotation, resulting from the mechanism mentioned above.

Case 1, Case 2 and Case 3 are also characterized by a different position of the saddle point along $\overline{z}$, see the blue star marker in Figures 9b, 9e and 9h. Case 1 and Case 2 feature a symmetric configuration of the wake, with the saddle point located at $\overline{z} \approx 0$ (see Figure 9b). Conversely, Case 3 displays a stronger disruption of the wake structure, with the saddle point being located at $\overline{z} > 0$.

Indeed, the observed activation of the top jet in Case 2 (see Tables III and IV), consequent to the alteration in the forcing conditions, reveals a critical mechanism in achieving a symmetrical wake configuration despite the differences in the lateral jet flow rate. This phenomenon elucidates the interplay between various flow control parameters and their impact on the wake structure. By strategically activating the top jet, compensatory flow adjustments are made, effectively counterbalancing the reduced flow rate from the side jets. Consequently, this coordination ensures the desired wake symmetry.

Observing the recirculation bubble highlighted in Figures 9a and 9b, a notable difference emerges between Case 1 and Case 2. In Case 1, the wake exhibits a greater extent in the $\overline{z}$ direction but a reduced streamwise extent compared to Case 2. This discrepancy can be attributed to the distinct forcing conditions outlined in Table III. Specifically, the higher flow rate induced by the lateral jets in Case 1 contributes to the

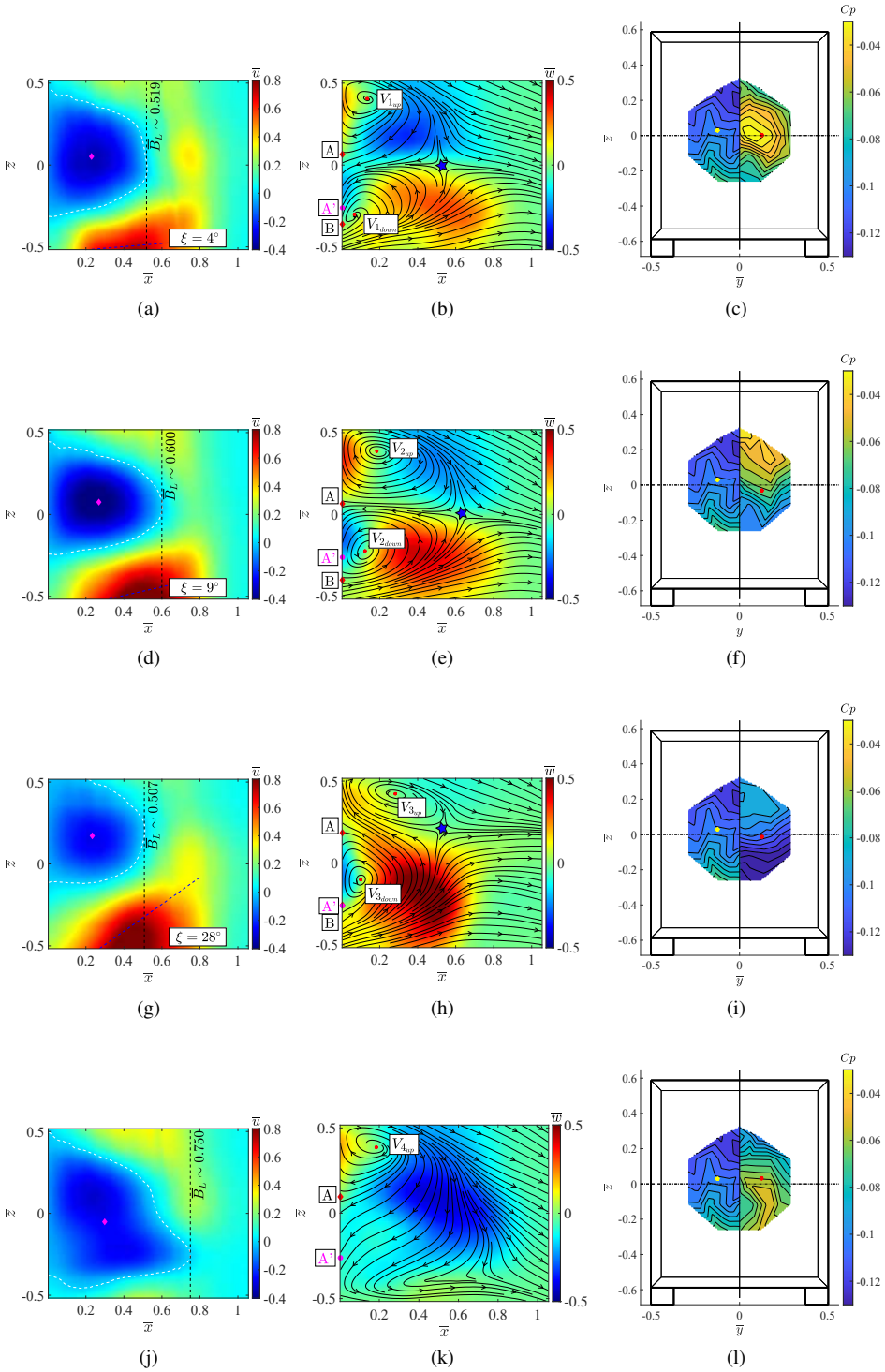

FIG. 9: Colormaps of the time averaged streamwise velocity component measured in the xz plane ($\overline{y}=0$) (a, d, g, j). The centroid of the wake is represented with a purple marker in (a), along with the iso-line of $\overline{u}=0$ (white dashed line) and the indication of the streamwise extent of the wake BL (black dashed line). Colormap of the time-averaged vertical velocity component, with overlaid $u-w$ streamlines, measured in the xz plane ($\overline{y}=0$) (b, c, h, k). Pressure coefficient measured across the model base (c, f, i, l): baseline (left side) and forced respectively on the left and right side, markers highlight $\overline{y_p}$ and $\overline{z_p}$. From top to bottom: Case 1 (a,b,c), Case 2 (d,e,f), Case 3 (g,h,i) and Case 4 (j,k,l). The blue star denotes the saddle point position. For each Case, point A and B represent the points of flow reattachment based on the model, while point A' represents the analogue for the baseline flow.

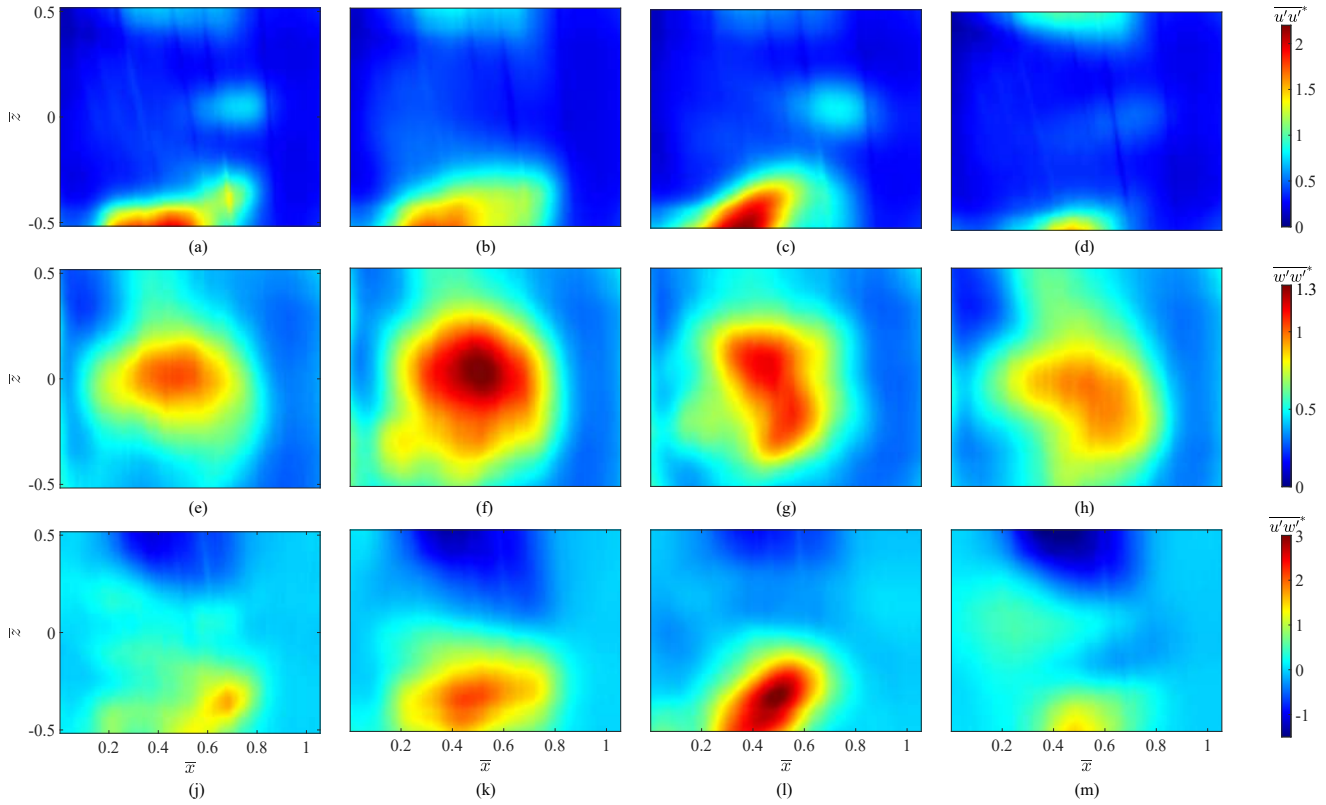

FIG. 10: Colormaps of the streamwise (a, b, c, d), cross-stream (e, f, g, h) components of the velocity variance, and streamwise-cross stream velocity covariance (i, j, k, l) measured in the xz plane ($\bar{y} = 0$). From left to right: Case 1, Case 2, Case 3 and Case 4.

development of the bubble predominantly in the $\bar{z}$ direction. Conversely, in Case 2, the activation of the upper jet introduces a new boundary, imposing constraints on the recirculation bubble's evolution. This, coupled with the lower lateral flow rate, leads to a more elongated bubble in the $\bar{x}$ direction. In the baseline case (see Figure 5b), the saddle point was not well resolved, but as observed in Wang *et al.*[39] on the same model, it is located at $\bar{z} \sim -0.2$ and $\bar{x} \sim 0.9$. By analyzing the forcing conditions, it can be inferred that the effect of the lower forcing is to move the saddle point upward. However, without lateral forcing, the wake fails to symmetrize (Case 3), as it can be inferred by comparing Figures 9b and 9e with Figure 9h. The effect of the lateral jet on the vertical position of the centroid of the recirculation bubble (Figures 9a, 9d, 9g and 9h), although counterintuitive, can be justified considering the existence of edge effects on the flow emerging from the jets. The centre section is approximately located at the centreline of the base. The lateral jets play a role in mitigating the effect of the bottom jet in displacing the near wake upwards (Case 1, Case 2 and Case 3, respectively in Figures 9b, 9e and 9h). As such, despite the bottom jet effect, for Case 4, the recirculation region extends further downwards as clearly shown in Figure 9j.

It is relevant to observe that, for the analyzed forcing conditions, there is a correlation between the position of the saddle point and the achieved drag reduction. The cases with the largest drag reduction are those with a more symmetric configuration of the wake in the xz plane (Case 1 and Case 2). Conversely, in Case 3, despite the saddle point approaching the base of the model, there is no symmetrization, and very low drag reduction values are measured.

The pressure coefficient distributions measured across the base of the model are reported in Figures 9c, 9f, 9i and 9l. These distributions, as in the case of a larger value of drag reduction (Case 1 and Case 2 respectively Figures 9c and 9f), involve significant pressure recovery and a reversal of the direction of the pressure gradient with respect to the baseline flow. The pressure recovery, compared to the baseline flow, is about $\sim 40\%$ in Cases 1 and 2 and about $\sim 16\%$ in Cases 3 and 4.

The components of the Reynolds stress tensor measured in the xz plane normalised with the maximum value of Reynolds stress for the baseline case, as shown in eq. 12, are reported in Figure 10.

$$\overline{u_i'u_j'}^* = \frac{\overline{u_i'u_j'}}{max(\overline{u_i'u_j'})_b} \tag{12}$$

where the subscript b stands for baseline case. Except for Case 4 (Figures 10d and 10h), where it was observed that the effect of the actuation in the xz plane is practically negligible, the streamwise ($\overline{u'u'}$, in Figures 10a, 10b, 10c and 10d) and vertical ($\overline{w'w'}$ in Figures 10e, 10f, 10g and 10h) components

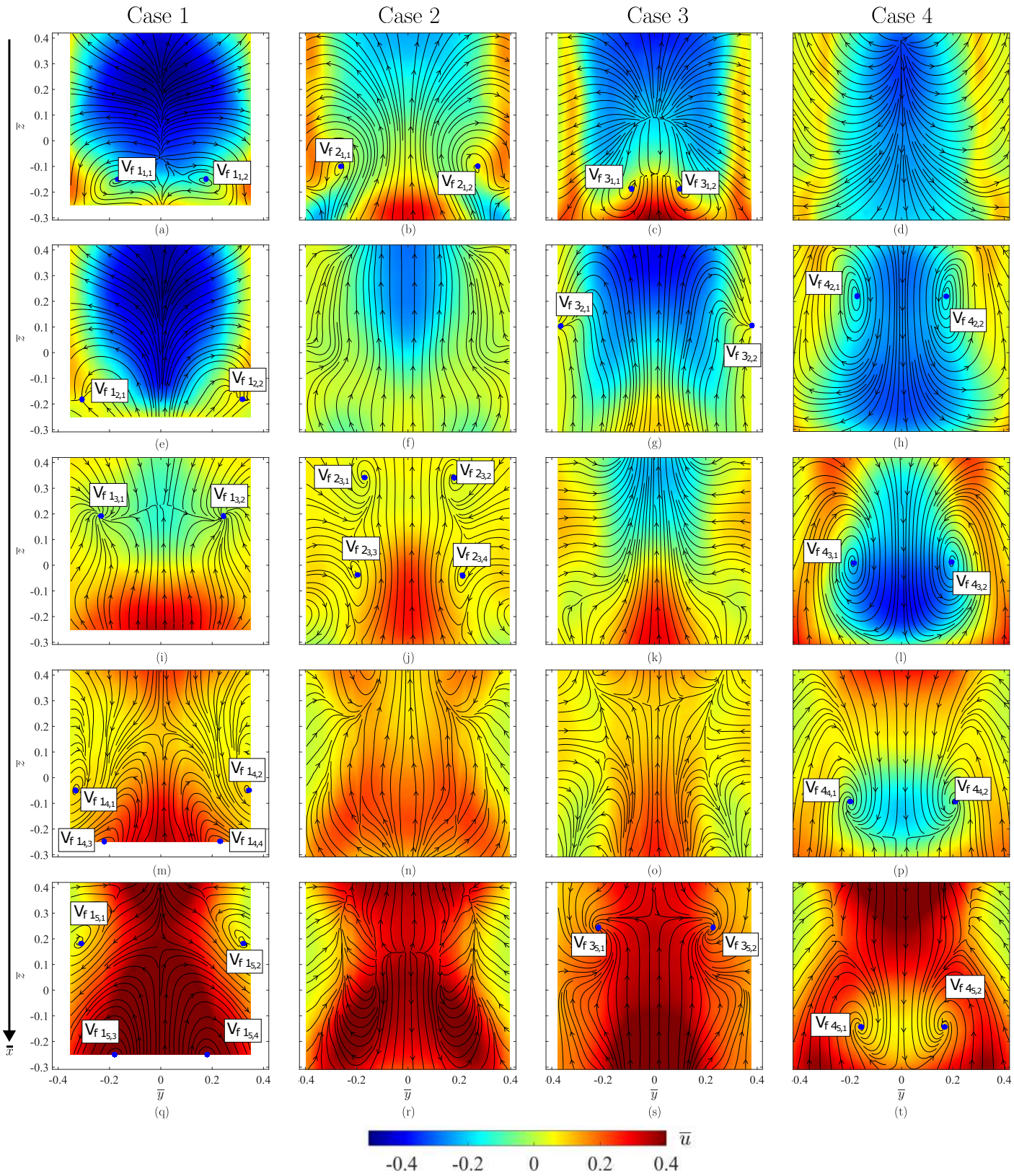

FIG. 11: Colormaps of streamwise velocity $\bar{u}$ field at $\bar{x} =$ 0.15 (a, b, c, d), 0.4 (e, f, g, h), 0.6 (i, j, k, l), 0.8 (m, n, o, p), 1.0 (q, r, s, t) with $v - w$ streamlines (in black).

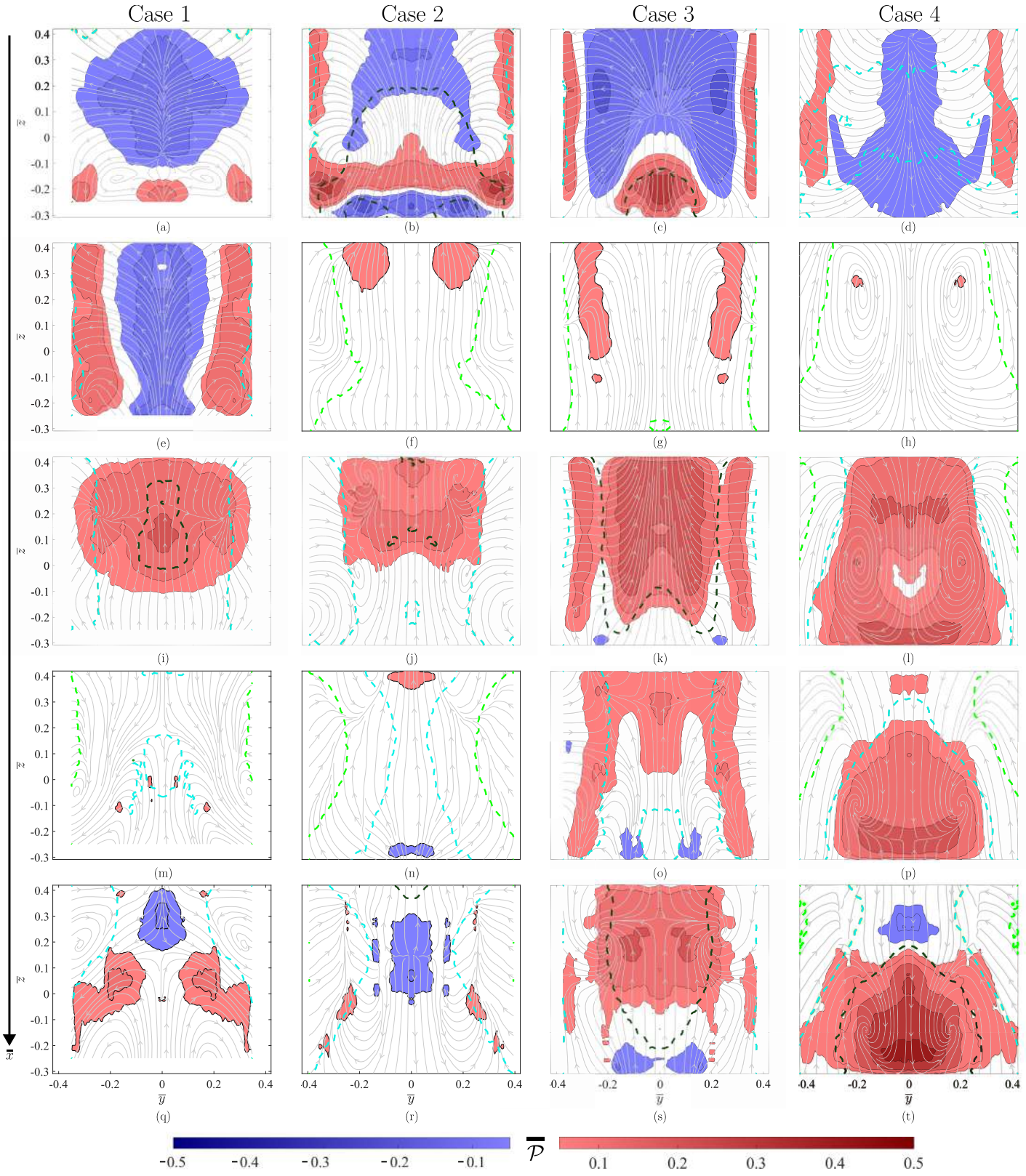

FIG. 12: Colormaps of $\overline{\mathcal{P}}$ field at $\overline{x} =$ 0.15 (a, b, c, d), 0.4 (e, f, g, h), 0.6 (i, j, k, l), 0.8 (m, n, o, p), 1.0 (q, r, s, t) with overlaid $v-w$ streamlines and $\overline{q^2}$ isolines for $\overline{q^2} = 0.08$ (light green), 0.15 (light blue), and 0.30 (dark green).

are intensified in the bottom region as a direct result of the shears generated by the bottom jet. Additionally, the increase in $\overline{w'w'}$ suggested greater wake meandering, attributable to lateral forcing. Meanwhile, the increased $\overline{u'w'}$ stress values (Figures 10i, 10l and 10m) indicate an intensification of the shear layer generated between the wake flow and the underbody flow.

From these analyses, it is evident that the introduction of a large flow rate modifies the shear layer that originates from the model edges, allowing for the anticipation of the closure of the recirculating area, as previously observed when discussing Figure 9. The results seem to confirm what was observed by Castelain et al.[4], who suggested that, if the underbody flow is characterized by low momentum, it is unable to remain attached to the ground and as a result, a direct backflow is generated towards the base with ground separation. By energizing the underbody flow, the flow has sufficient momentum to be channelled along the ground and avoid separation to withstand the strong adverse pressure gardient at the base.

Figure 11 shows the sPIV fields of the streamwise velocity component measured at $\overline{x} = 0.15, 0.4,\ 0.6,\ 0.8$ and 1.0 with overlaid streamlines of the inplane velocity components. By examining Figure 11, it becomes clear that the source, present in the baseline case (Figure 6a also reported in Cerutti *et al.* [12]), appears severely modified. In Case 1 and Case 2, in fact, as a consequence of the bubble shift towards the base of the model, the source gets closer to the wall.

The imprinting of the forcing can also be observed in terms of production $\overline{\mathcal{P}}$ and turbulent kinetic energy $\overline{q^2}$ (see Figure 12). For Case 1, Case 2 and Case 3, the large flow injection through the bottom jet leads to an increased production for $\overline{z} < 0$ at $\overline{x} = 0.15$ (see Figures 12a, 12b, and 12c) with peaks approximately located within $-0.2 < \overline{z} < 0$. This is reasonable considering the jet arrangement, as described in Tab. II, with an injection angle of 65° with respect to the xy plane. Additionally, the larger values of production evidenced at $\overline{x} = 0.6$ (see Figures 12i, 12j and 12k) are a consequence of the early closure of the recirculation bubble. As depicted in Figures 12a, 12b and 12c, there are intense and shifted peaks of production towards the midplane xz as a consequence of the lateral forcing. Regarding $\overline{q^2}$, three different values of the turbulence kinetic energy $\overline{q^2}$ are represented by isolines in the Figure 12, $\overline{q^2} = 0.08$ (light green), 0.15 (light blue), and 0.30 (dark green). High values of $\overline{q^2}$ are observed for the section closer to the base at $\overline{x} = 0.15$ and $\overline{x} = 0.4$. This can be justified despite the expected increase in pressure being followed by a decrease in $\overline{q^2}$. This is because of the higher negative $\overline{w}$ values. The forcing pushes the recirculation bubble towards the base of the model, as evidenced in Figure 9d, 9g and 9j, resulting in a strong transfer of turbulent kinetic energy to the mean flow in this region. Therefore, it appears that, under maximum drag reduction conditions, the imposed forcing generates a region near the model's base characterized by intense turbulent activity. In this zone, energy is extracted from the mean flow, facilitating the early closure of the wake and subsequently reducing the values of $\overline{q^2}$ and $\overline{\mathcal{P}}$ for sections located far from the model's base, see Figure 12.

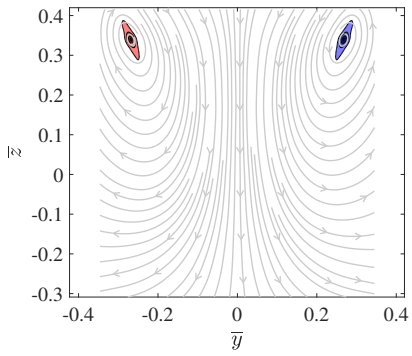

FIG. 13: Example of the application of Γ_1 for vortex core identification. This example is referred to the baseline Case for $\overline{x} = 0.4$. The colormap denotes $\Gamma_1 > 0.5$ in red, and $\Gamma_1 < -0.5$ in blue, with overlaid $v - w$ streamlines (in gray).

C. FLOW CONTROL MECHANISMS

To comprehend the mechanisms by which DRL agents achieve their goals, we hereby compare the baseline flow with the forced flows. To highlight the flow structures, the Γ_1 [50,51] criterion was used. Namely, setting Γ_1 equal to 0.5, it was possible to identify the core of the vortex structures.

The outcomes of the $\Gamma 1$ analysis are shown in Figure 13, for one representative case (baseline case at $\overline{x} = 0.4$), while the results for all the other cases are reported only with the schematics of Figure 14.

In this section we introduce the following labeling of the vortical structures identified in the time-averaged sPIV measurements of Figure 11: Vfk_i, j indicates $j-th$ vortical structure identified at the $i-th$ streamwise plane, the subscript f indicates $k-th$ forced case and b subscript the baseline one.

As shown in Figure 6a, the flow exhibits vortices ($Vb_{2,1}$ and $Vb_{2,2}$) at the edges of the region where $\overline{u} \sim 0$, extending in the streamwise direction. From $\overline{x} = 0.4$ to $\overline{x} = 0.8$ (see Figures 11b, 11c, 11d and 11e), the identified structures ($Vb_{3,1}$,$Vb_{3,2}$, $Vb_{4,1}$ and $Vb_{4,2}$) exhibit coherence in the streamwise direction. These structures are generated by the roll-up of the wake detaching from the corners of the upper trailing edge. These vortices are commonly referred to as C-Pillar vortices[39].

They surround the recirculation zone, as shown in Figures 6b, 6c and 6d. It can also be observed that these structures tend to grow in the streamwise direction as they entrain mass from the surroundings while they eventually undergo viscous dissipation farther downstream. Additionally, the centers of the vortical structures tend to move downward and toward the symmetry plane until the bubble closes. Further downstream then they tend to move outward (see Figures 6d and 6e). This phenomenon is evident at $\overline{x} = 1.0$, where the recirculation bubble is closed.

Starting from $\overline{x} = 0.8$ (see Figures 6d and 6e), an upward-directed flow is observed for $\overline{z} < 0$. This is likely the flow originating from the detachment of the lower bubble (see Figure 4a and 4b).

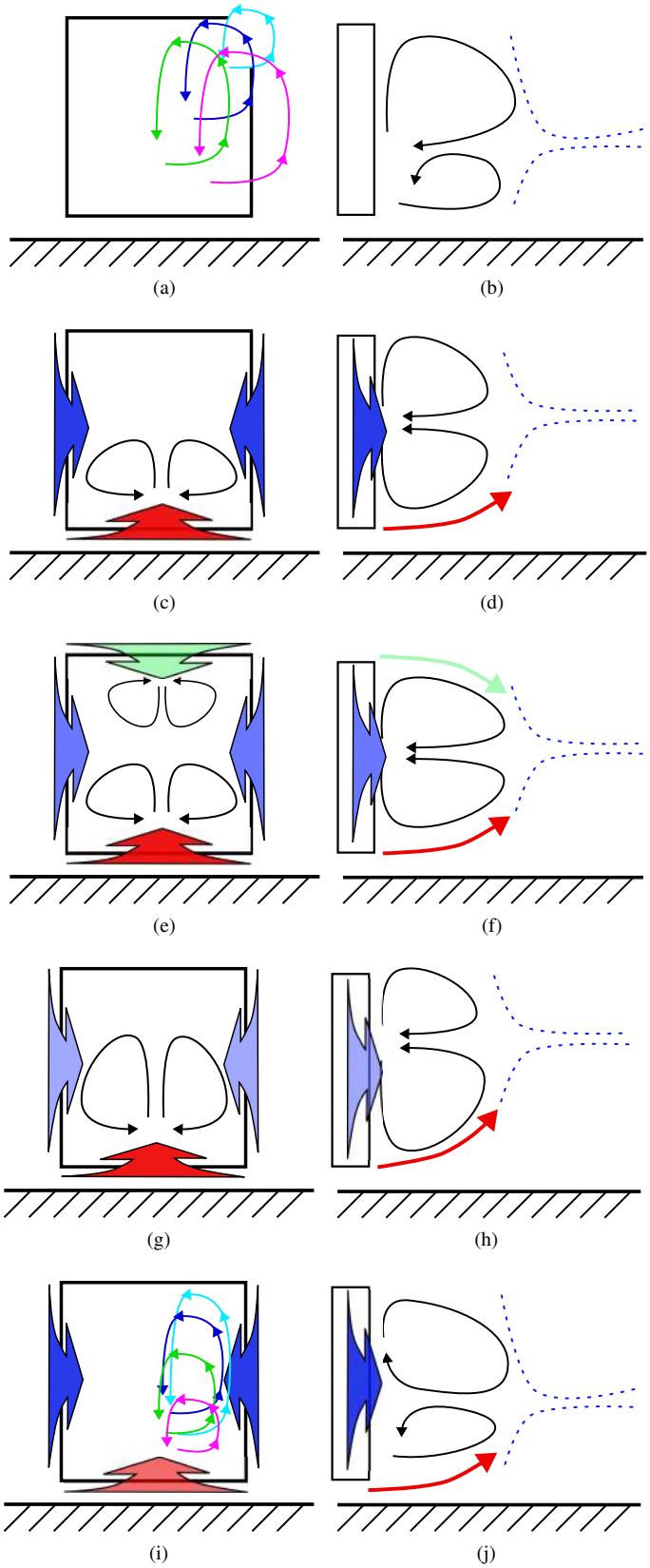

FIG. 14: Schematic representation of the wake for the baseline case (a and b), Case 1 (c and d), Case 2 (e and f), Case 3 (g and h) and Case 4 (i and j). Rear views from downstream (left columns) and side views from the left side (right columns). For the forced cases,the side jets are shown with blue arrows, the top jets with green arrows and the bottom jets with red arrows. The color intensity qualitatively describes the jet amplitude with darker colors representing larger amplitudes. The structures highlighted in (a) and (i) are color-coded by the different investigation plane.

Analyzing the forced conditions, a first point to take into account is the existence of vortical structures with vorticity of opposite sign compared to the baseline case in Cases 1, 2, and 3 (refer to Figure 11, for examples $Vf1_{1,1}$, $Vf2_{1,1}$, and $Vf3_{1,1}$), but this phenomenon is not observed in Case 4. This can be explained by examining the forcing conditions (refer to Tables II and III). The reversal in the sign of vorticity can be attributed to the influence of the bottom jet. This statement becomes understandable when taking into account the edge effects of the bottom jet, which result in a higher flow rate in the central region compared to the peripheral areas. When the incoming flow from the bottom jet encounters a flow in the opposite direction, a saddle point is formed. Consequently, a recirculation zone is created, similar to what occurs with a cross-flow jet[52].

In Case 1, as depicted in Figure 11a, the phenomenon described in the previous paragraph becomes evident. Two vortical structures ($Vf1_{1,1}$ and $Vf1_{1,2}$) with $\overline{\omega_x} < 0$ for $\overline{y} > 0$ are observed, as also sketched in Figure 14c. The vortices present in the baseline case are significantly reduced in size, and their presence is not visible within the measurement plane. However, at $\overline{x} = 0.6$, in Figure 11i, two structures become noticeable for $\overline{y} = 0.15$. They could be attributed to the aforementioned vortices resulting from the flow detachment from the model's roof, which coalesce with the structures resulting from the closure of the recirculation zone[3]. As observed for the baseline case, these structures tend to develop in the streamwise direction, coexisting with the structures ($Vf1_{5,3}$,$Vf1_{5,4}$) originating from the interaction beteween the underbody flow and the bottom jet (see Figure 11i).

In contrast to the baseline case, the lateral structures identified at $\overline{x} = 0.8$ and 1.0 (see Figures 11m and 11q) may not be solely attributed to the detachment of the flow from the side walls of the model. The lateral jets narrow the recirculation zone (see Figure 11e). Consequently, the flow tends to twist, giving rise to a vortical structure that intervenes between the lateral vortices and the recirculation bubble.

As noted earlier, for both Case 1 and Case 2, the presence of structures $V_{f2_{1,1}}$ and $V_{f2_{1,2}}$ (refer to Figure 11b) is evident, which can be attributed to the interaction between the lower jet and the recirculation bubble. However, it is crucial to highlight the presence of structures $V_{f2_{3,1}}$ and $V_{f2_{3,2}}$ in Figures 11j for Case 2. These structures exhibit a vorticity opposite in sign to those identified for the baseline flow, represented by $V_{b2,1}$ and $V_{b2,2}$ in Figure 11b. The appearance of $V_{f2_{3,1}}$ and $V_{f2_{3,2}}$ can be explained by considering the introduction of flow from the top jet for Case 2. Similar to the mechanism described earlier for the bottom jet, the interaction between the jet outflow and the recirculation bubble gives rise to these structures. An outline of what has been said so far is shown in the sketches of Figures 14e, 14f and 15c. Although the mechanism is the same, the structures related to the bottom jet are evident as early as $\overline{x} = 0.2$, see $Vf2_{2,1}$ and $Vf2_{2,1}$ in Figure 11b, while those related to the top jet are only evident from $\overline{x} = 0.6$, see Figure 11j. This is motivated by considering that the forcing related to the bottom jet is much more intense than the top jet, see Table III. For Case 2, where the C-pillars are not visible within the investigation region, it is reasonable to state that the structures $V_{f2_{2,1}}$ and $V_{f2_{2,2}}$ intervene between the recirculation bubble and the C-pillar. Consequently, these structures effectively displace the C-pillars beyond the investigated region.

A reduced mass flow rate from the bottom jet allows the entry of the vortical structures originating from the model's roof within the imaged area. Furthermore, in Case 2 at $x = 0.6$ (see Figure 11j) a pair of vortices is clearly visible. These vortices are likley originated from the front wheels, as suggested by Wang *et al.* [39]. These, as reported in[39], are localized for $|\overline{y}| > 0.5$ and thus are not visible in the investigated region. Instead, here (Case 2) the presence of a more flattened inward wake draws these structures inward.

Case 3 and Case 4 are also of particular interest since their forcing conditions reflect those identified by the agent when energy budget considerations were accounted for in the reward definition. For Case 3, as sketched in Figures 14g and 14h, the bottom jet injects flow at a higher angle relative to the streamwise direction compared to the previous case (Case 2), see Figures 9a, 9d, 9g and 9j, as previously discussed. For Case 1 and Case 2, the lateral forcing was particularly intense (see Table III), causing the outflow from the bottom jet to deviate. As a result of lower flow rate from the side jets, there is an upstream shift of the recirculating flow ($\overline{B}_L \approx 0.507$, see Figure 9g). Simultaneously, it introduces an upstream shift in the formation of the lower vortex structures observed for Cases 1 and 2 (see Figure 9c). These structures are likely a consequence of the interaction between the high-speed flow originating from the underbody and the flow from the bottom jet. Comparing the three cases examined so far (Case 1, Case 2 and Case 3), it can be stated that the upstream shift of the recirculation bubble closure is primarily influenced by the lower jet.

Moving downstream (see Figures 11o and 11s), it is observed that for $\overline{y} > 0$, structures that could be attributed to the C-pillar vortices become evident with an upward shift of these structures.

A schematic representation of the wake characteristics for Case 4 is shown in Figure 14g and 14h. The forcing from the bottom jet is minimal, unlike the lateral forcing, as evident in Figures 11d and 11h where the lateral compression of the recirculation zone is noticeable. It is crucial to note that the structures present, however, are comparable to what was observed for the baseline case with a shift toward $\overline{y} \sim 0$.

The lateral forcing introduces momentum near the centerline. While this does not lead to an upstream shift in the closure of the recirculation bubble, it does bring the vortex core (see Figure 9k) closer to the base of the model and causes it to shift upward. Consequently, there is a shift of the stagnation point to $\overline{z} > 0$, as observed in the shift between A' and A (see Figure 9k). This shift leads to a recovery of pressure and consequently to a reduction in drag.

IV. CONCLUSIONS

In this study, the wake topology of a road-vehicle model manipulated with pulsed jets was investigated by means of planar and stereoscopic PIV. The control laws were defined

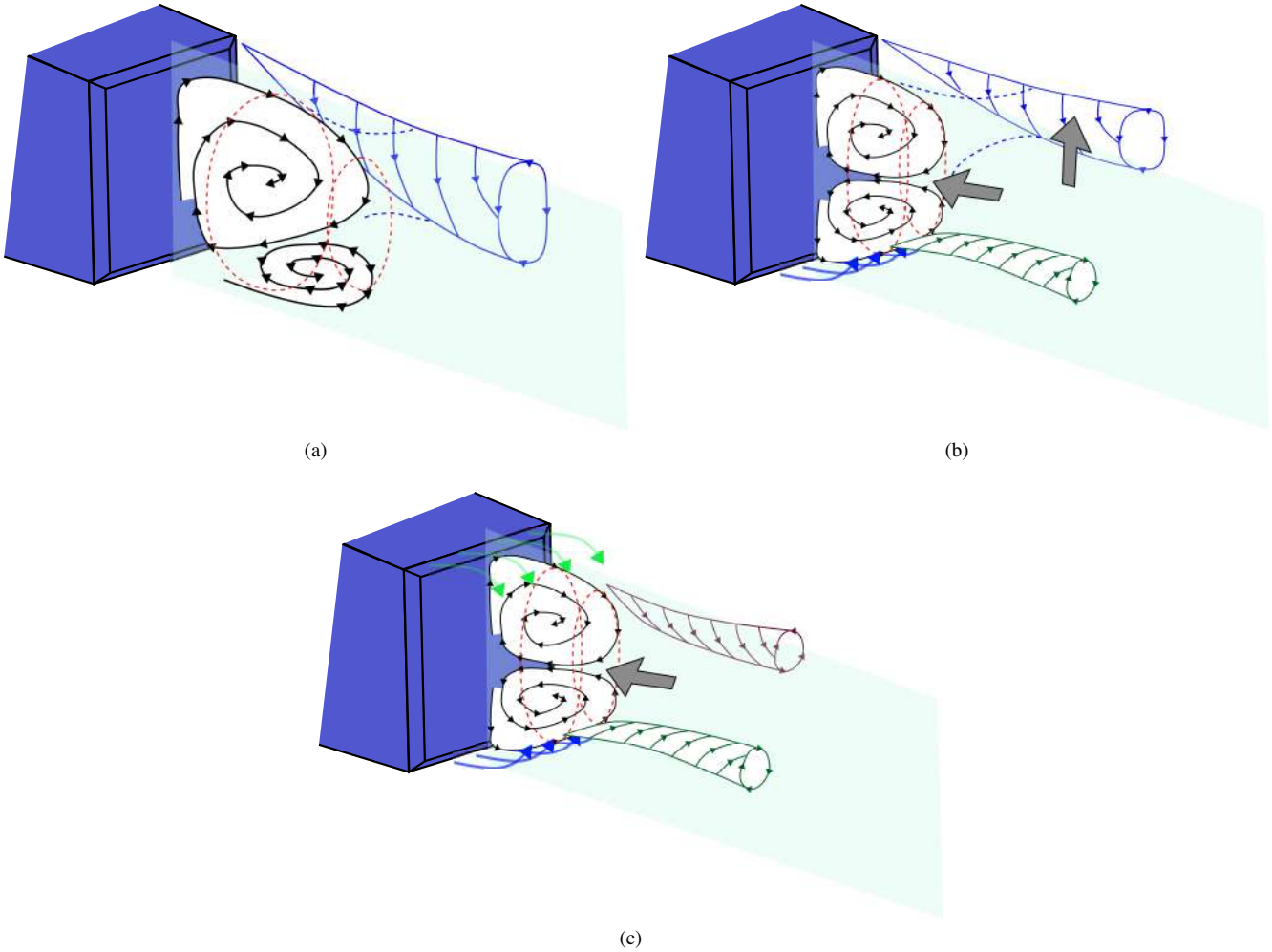

FIG. 15: Schematic representation of the wake for Baseline Case (a) and forced case under maximum drag reduction conditions (b and c).

for training a DRL agent, aimed at maximizing a reward based either on the drag reduction alone or accounting also for the efficiency in the actuation.

The conditions that achieve significant drag reduction are characterized by a large pressure recovery at the base of the model. The extent of the recirculating region is shortened with respect to the unforced case, with values of $\overline{B}_L$ reducing from 0.8 down to 0.5 and 0.6, respectively in Case 1 and Case 2. Furthermore, the vortical structures in the xz plane attain a symmetric configuration, with a saddle point that shifts upward toward the centre of the wake. The model sketched in Figures 15b and 15c, shows the wake configuration under the maximum drag reduction condition, Case 1 and 2. It is possible to observe an upward shift of the C-pillar and a compression of the recirculation bubble toward the model's base, leading to larger pressure recovery, can be observed. The interaction of the underbody flow with the recirculation bubble creates a vortex structure that evolves in the streamwise direction. In Case 1, a discernible upward displacement of the C-pillar and compression of the bubble towards the model's base are evident, leading to a larger pressure recovery. Additionally, for Case 2, the emergence of structures associated with the interaction between the top jet and the recirculation bubble is observed. Through the conducted analyses, it becomes apparent that the agent can identify the condition of maximum drag reduction, characterized by wake symmetrization, and achieves this configuration using different control laws. Notably, for Case 2, that agent substitutes the flow reduction from the side jet with the synchronized activation of the top jet.

In contrast, the conditions that took the energy budget into account (Case 3 and 4) showed a wake more similar to the natural with a streamwise extent of the recirculation bubble ranging from $\overline{B}_L = 0.5$W to $\overline{B}_L = 0.75$W, respectively for Case 3 and Case 4. Nevertheless, for Case 3, the wake, retains a symmetrical configuration in the xz plane.

These results suggest that the flow injection from the bottom jet is an effective way to achieve drag reduction ($\sim 10\%$), as it anticipates the closure of the recirculating zone by moving the interaction between the shear layers generated by the top and bottom model edges further upstream. However, this method requires significant energy consumption.

On the other hand, lateral flow injection can achieve good drag reduction values ($\sim 5\%$) with less energy expenditure by relying on the symmetry of the wake on the vertical plane rather than modifying the interaction of the shear layers.

Further investigations are needed to gain a deeper understanding of the underlying mechanisms of the achieved control, by investigating the aspect related to the dynamic evolution of the flow. However, it is important to note that during evaluation, as reported in Amico et al.[35], each agent adopts a forcing configuration that it tries to maintain throughout the episode. This is a result of greedy training, as the implementation follows a one-step Deep Reinforcement Learning approach. Undoubtedly, the lack of foresight from the agent leads to a failure to explore potentially more complex dynamics compared to a one-step approach, which could result in greater drag reduction. On the other hand, having found a single forcing condition for each agent that leads to a suboptimal condition allows for the exploitation of this configuration in open-loop approaches. Furthermore, the use of a data-based approach allows for the generation of a large dataset of states at the end of the training, specifically for this work, the pressure distribution on the model base, which can be used to modify the model geometry and thus to obtain passive control techniques.

ACKNOWLEDGEMENTS

The authors wish to thank Prof. T. Astarita for providing the software used to acquire and process the PIV and sPIV images.

DATA AVAILABILITY

The data that support the findings of this study are available from the corresponding author upon reasonable request.

[1]Z. Mohamed-Kassim and A. Filippone, "Fuel savings on a heavy vehicle via aerodynamic drag reduction," Transportation Research Part D: Transport and Environment **15**, 275–284 (2010), 10.1016/J.TRD.2010.02.010.

[2]P. Gilliéron and A. Kourta, "Aerodynamic drag reduction by vertical splitter plates," Experiments in Fluids **48**, 1–16 (2009), 10.1007/s00348-009-0705-7.

[3]K. Liu, B. F. Zhang, Y. C. Zhang, and Y. Zhou, "Flow structure around a low-drag ahmed body," Journal of Fluid Mechanics **913**, A21 (2021), 10.1017/jfm.2020.1136.

[4]T. Castelain, M. Michard, M. Szmigiel, D. Chacaton, and D. Juvé, "Identification of flow classes in the wake of a simplified truck model depending on the underbody velocity," Journal of Wind Engineering and Industrial Aerodynamics **175**, 352–363 (2018), 10.1016/J.JWEIA.2018.02.004.

[5]M. Grandemange, O. Cadot, and M. Gohlke, "Reflectional symmetry breaking of the separated flow over three-dimensional bluff bodies," Physical Review E **86**, 35302 (2012), 10.1103/PhysRevE.86.035302.

[6]G. Bonnavion and O. Cadot, "Unstable wake dynamics of rectangular flat-backed bluff bodies with inclination and ground proximity," Journal of Fluid Mechanics **854**, 196–232 (2018), 10.1017/jfm.2018.630.

[7]D. Barros, J. Borée, B. R. Noack, A. Spohn, and T. Ruiz, "Bluff body drag manipulation using pulsed jets and coanda effect," Journal of Fluid Mechanics **805**, 422–459 (2016), 10.1017/jfm.2016.508.

[8]M. Grandemange, M. Gohlke, and O. Cadot, "Turbulent wake past a three-dimensional blunt body. part 1. global modes and bi-stability," Journal of Fluid Mechanics **722**, 51–84 (2013), 10.1017/jfm.2013.83.

[9]M. Grandemange, M. Gohlke, and O. Cadot, "Bi-stability in the turbulent wake past parallelepiped bodies with various aspect ratios and wall effects," Physics of Fluids **25**, 095103 (2013), 10.1063/1.4820372.

[10]O. Evstafyeva, A. S. Morgans, and L. D. Longa, "Simulation and feedback control of the ahmed body flow exhibiting symmetry breaking behaviour," Journal of Fluid Mechanics **817**, 817R21–817R212 (2017), 10.1017/jfm.2017.118.

[11]C. Chen, S. Wang, and S. Ghaemi, "Spectral proper orthogonal decomposition of time-resolved three-dimensional flow measurements in the turbulent wake of the ahmed body," Journal of Fluid Mechanics **985**, A19 (2024), 10.1017/jfm.2024.288.

[12]J. J. Cerutti, C. Sardu, G. Cafiero, and G. Iuso, "Active flow control on a square-back road vehicle," Fluids **5** (2020), 10.3390/fluids5020055.

[13]J. J. Cerutti, G. Cafiero, and G. Iuso, "Aerodynamic drag reduction by means of platooning configurations of light commercial vehicles: A flow field analysis," International Journal of Heat and Fluid Flow **90** (2021), 10.1016/j.ijheatfluidflow.2021.108823.

[14]G. Iuso, "Base pressure control by passive methods," 18th Fluid Dynamics and Plasmadynamics and Lasers Conference 10.2514/6.1985-1620.

[15]M. Minguez, R. Pasquetti, and E. Serre, "High-order large-eddy simulation of flow over the "ahmed body" car model," Physics of Fluids **20** (2008), 10.1063/1.2952595.

[16]A. Spohn and P. Gilliéron, "Flow separations generated by a simplified geometry of an automotive vehicle flow separations on the ahmed body flow separations generated by a simplified geometry of an automotive vehicle," (2002).

[17]S. Krajnović and L. Davidson, "Flow around a simplified car, part 2: Understanding the flow," (2005) pp. 919–928, 10.1115/1.1989372.

[18]G. Franck, N. Nigro, M. Storti, and J. D'Elía, "Numerical simulation of the flow around the ahmed vehicle model," Latin American Applied Research **39**, 295–306 (2009).

[19]X. Wang, Y. Zhou, Y. Pin, and T. Chan, "Turbulent near wake of an ahmed vehicle model," Experiments in Fluids **54** (2013), 10.1007/s00348-013-1490-x.

[20]S. R. Ahmed, G. Ramm, and G. Faltin, "Some salient features of the time-averaged ground vehicle," (1984).

[21]H. Lienhart and S. Becker, "Flow and turbulence structure in the wake of a simplified car model," (2003).

[22]B. F. Zhang, Y. Zhou, and S. To, "Unsteady flow structures around a high-drag ahmed body," Journal of Fluid Mechanics **777**, 291–326 (2015), 10.1017/jfm.2015.332.

[23]J. Venning, D. L. Jacono, D. Burton, M. C. Thompson, and J. Sheridan, "The nature of the vortical structures in the near wake of the ahmed body," Proceedings of the Institution of Mechanical Engineers, Part D: Journal of Automobile Engineering **231**, 1239–1244 (2017), 10.1177/0954407017690683.

[24]G. Minelli, T. Dong, B. R. Noack, and S. Krajnović, "Upstream actuation for bluff-body wake control driven by a genetically inspired optimization," Journal of Fluid Mechanics **893** (2020), 10.1017/jfm.2020.220.

[25]R. Castellanos, G. Y. C. Maceda, I. de la Fuente, B. R. Noack, A. Ianiro, and S. Discetti, "Machine-learning flow control with few sensor feedback and measurement noise," Physics of Fluids **34**, 047118 (2022), 10.1063/5.0087208.

[26]J. Rabault, M. Kuchta, A. Jensen, U. Réglade, and N. Cerardi, "Artificial neural networks trained through deep reinforcement learning discover control strategies for active flow control," Journal of Fluid Mechanics **865**, 281–302 (2019), 10.1017/jfm.2019.62.

[27]L. Guastoni, J. Rabault, P. Schlatter, H. Azizpour, and R. Vinuesa, "Deep reinforcement learning for turbulent drag reduction in channel flows," European Physical Journal E **46** (2023), 10.1140/epje/s10189-023-00285-8.

[28]R. Li, D. Barros, J. Borée, O. Cadot, B. R. Noack, and L. Cordier, "Feedback control of bimodal wake dynamics," (2016), 10.1007/s00348-016-2245-2.

[29]C. Vignon, J. Rabault, J. Vasanth, F. Alcántara-Ávila, M. Mortensen, and R. Vinuesa, "Effective control of two-dimensional rayleigh-bénard convection: Invariant multi-agent reinforcement learning is all you need," Physics of Fluids **35** (2023), 10.1063/5.0153181.

[30]D. Fan, L. Yang, Z. Wang, M. S. Triantafyllou, and G. E. Karniadakis, "Reinforcement learning for bluff body active flow control in experiments and simulations," Proceedings of the National Academy of Sciences **117**,

26091–26098 (2020), 10.1073/pnas.2004939117.
[31]L. Yan, Y. Li, G. Hu, W. li Chen, W. Zhong, and B. R. Noack, "Stabilizing the square cylinder wake using deep reinforcement learning for different jet locations," Physics of Fluids **35**, 115104 (2023), 10.1063/5.0171188.
[32]H. Zong, Y. Wu, H. Liang, Z. Su, and J. Li, "Experimental study on q-learning control of airfoil trailing-edge flow separation using plasma synthetic jets," Physics of Fluids **36**, 015101 (2024), 10.1063/5.0185853.
[33]C. Xia, J. Zhang, E. C. Kerrigan, and G. Rigas, "Active flow control for bluff body drag reduction using reinforcement learning with partial measurements," (2023).
[34]S. Shimomura, S. Sekimoto, A. Oyama, K. Fujii, and H. Nishida, "Closed-loop flow separation control using the deep q network over airfoil," AIAA Journal **58**, 4260–4270 (2020), 10.2514/1.J059447.
[35]E. Amico, G. Cafiero, and G. Iuso, "Deep reinforcement learning for active control of a three-dimensional bluff body wake," Physics of Fluids **34**, 105126 (2022), 10.1063/5.0108387.
[36]Englar, Robert J., "Advanced aerodynamic devices to improve the performance, economics, handling and safety of heavy vehicles," *SAE International Government/Industry Meeting*, (2001), https://doi.org/10.4271/2001-01-2072.
[37]J. J. Cerutti, "Aerodynamics of a squareback road vehicle with active flow control," Doctoral thesis Politecnido di Torino (2020).
[38]A. Capone and G. P. Romano, "Investigation on the effect of horizontal and vertical deflectors on the near-wake of a square-back car model," Journal of Wind Engineering and Industrial Aerodynamics **185**, 57–64 (2019), 10.1016/j.jweia.2018.12.011.
[39]J. Wang, G. Minelli, G. Cafiero, G. Iuso, K. He, B. Basara, G. Gao, and S. Krajnović, "Validation of pans and effects of ground and wheel motion on the aerodynamic behaviours of a square-back van," Journal of Fluid Mechanics **958** (2023), 10.1017/jfm.2023.47.
[40]E. Amico, D. D. Bari, G. Cafiero, and G. Iuso, "Genetic algorithm-based control of the wake of a bluff body," (Institute of Physics, 2022) 10.1088/1742-6596/2293/1/012016.
[41]R. S. Sutton and A. G. Barto, "Reinforcement learning: An introduction second edition, in progress,".
[42]H. Dong, Z. Ding, S. Zhang, E. Fundamentals, and A. Research, "Deep reinforcement learning,".
[43]M. A. Mendez, M. Raiola, A. Masullo, S. Discetti, A. Ianiro, R. Theunissen, and J. M. Buchlin, "Pod-based background removal for particle image velocimetry," Experimental Thermal and Fluid Science **80**, 181–192 (2017), 10.1016/j.expthermflusci.2016.08.021.
[44]T. Astarita and G. Cardone, "Analysis of interpolation schemes for image deformation methods in piv," Experiments in Fluids **38**, 233–243 (2005), 10.1007/s00348-004-0902-3.
[45]T. Astarita, "Analysis of velocity interpolation schemes for image deformation methods in piv," Experiments in Fluids **45**, 257–266 (2008), 10.1007/s00348-008-0475-7.
[46]T. Astarita, "Analysis of weighting windows for image deformation methods in piv," Experiments in Fluids **43**, 859–872 (2007), 10.1007/s00348-007-0314-2.
[47]C. Willert, "Stereoscopic digital particle image velocimetry for application in wind tunnel flows," Measurement Science and Technology **8**, 1465 (1997), 10.1088/0957-0233/8/12/010.
[48]B. Wieneke, "Stereo-piv using self-calibration on particle images," (2005) pp. 267–280, 10.1007/s00348-005-0962-z.
[49]Y. Haffner, T. Castelain, J. Borée, and A. Spohn, "Manipulation of three-dimensional asymmetries of a turbulent wake for drag reduction," Journal of Fluid Mechanics **912** (2021), 10.1017/jfm.2020.1133.
[50]F. D. Gregorio, A. Visingardi, and G. Iuso, "An experimental-numerical investigation of the wake structure of a hovering rotor by piv combined with a $\gamma 2$ vortex detection criterion," Energies **14** (2021), 10.3390/en14092613.
[51]P. Chakraborty, S. Balachandar, and R. J. Adrian, "On the relationships between local vortex identification schemes," Journal of Fluid Mechanics **535**, 189–214 (2005), 10.1017/S0022112005004726.
[52]T. Berk and B. Ganapathisubramani, "Effects of vortex-induced velocity on the development of a synthetic jet issuing into a turbulent boundary layer," Journal of Fluid Mechanics **870**, 651–679 (2019), 10.1017/jfm.2019.279.